Passive Seismic Tomography Using Induced Seismicity at a Petroleum Field in Oman

Haijiang Zhang, Sudipta Sarkar, M. Nafi Toksoz, and H. Sadi Kuleli

Earth Resources Laboratory
Department of Earth, Atmospheric and Planetary Sciences
Massachusetts Institute of Technology
Cambridge, Massachusetts

Fahad Al-Kindy

Integrated Reservoir Monitoring
Reservoir Characterization Team (GN118)
Petroleum Development Oman
Muscat, Sultanate of Oman

Prepared for

Geophysics imaging/inversion special section

Revised on May 19, 2009

ABSTRACT

A borehole network consisting of 5 monitoring wells was used to monitor the induced seismicity at a producing petroleum field for a period of about 11 months. Nearly 5400 microseismic events were analyzed and utilized in imaging the reservoir based on a new double-difference (DD) seismic tomography. The DD tomography method simultaneously solves for event locations and Vp, Vs, and Vp/Vs models using absolute and differential P, S and S-P arrival times. Microseismicity in the field was primarily caused by compaction of the reservoir in and above the gas bearing formation and was distributed along the two major northeast-southwest (NE-SW) faults in the field. The model resolution analysis based on the checkerboard test and the resolution matrix showed that the central part of the model was relatively well resolved for the depth range of 0.7 to 1.1 km. Clear velocity contrasts were imaged across most parts of the two NE-SW faults. Vp/Vs ratio estimations from the tomographic inversion were low (<1.75) in the shallow depth range, likely due to lithology and gas content, whereas they were large (>1.75) in the deeper part of the model, likely due to fluid saturated formation. In this study seismic tomography showed a great potential for reservoir imaging and property estimation using induced seismicity.

INTRODUCTION

In the petroleum industry, induced seismicity has been mainly used as a monitoring tool, including hydraulic fracturing (e.g. Rutledge and Phillips, 2003), well/casing failure (e.g. Kristansen *et al.*, 2000), fault mapping (e.g. Maxwell *et al.*, 1998), mapping fluid movements (e.g. Rutledge et al., 1998), mapping compaction strains (e.g. Grasso, 1992), mapping thermal fronts (e.g. McGillivray, 2004), tracking fluid/steam injection (e.g. Deflandre *et al.*, 1995; Maxwell et al., 2008), and mapping waste disposals (e.g. Keck and Withers, 1994). At present, the majority of passive seismic monitoring applications in the petroleum industry are related to hydrofrac mapping. Monitoring of the associated microseismicity during a fracturing operation can give important insight into the fracture pattern and fluid migration. Similarly, monitoring of the seismic events that may be induced during the production-cycle of the field can be used to obtain valuable information about fluid movements and reservoir property changes in the reservoir. Although the number of such applications is very limited at the moment, with improvements in data acquisition and processing technology and better understanding of reservoir physics, usage of induced seismicity as a tool for reservoir monitoring and characterization is likely to flourish. Currently, the majority of passive seismic monitoring applications are built on locating and tracking induced microseismic events (e.g. Sze, 2005; Sarkar, 2008). In this paper, we show an example of how induced seismic events can add value to reservoir monitoring, beyond just locations, by doing reservoir imaging.

The field referenced in this study, operated by Petroleum Development Oman (PDO), was discovered in 1962 and put into production in 1969. An official program to monitor induced seismicity and subsidence in the field commenced in 1999 and a borehole network was installed in February of 2002. The primary objective of this passive seismicity monitoring program has been to locate the events, and to correlate them with production and injection activities in order to understand and monitor the cause of induced seismicity in the field. In this paper, we utilized the microseismic events recorded by the borehole network to image the three-dimensional seismic velocity structure around the reservoir. We employed a new version of the double-difference seismic travel time tomography method (Zhang and Thurber, 2003) that is able to simultaneously solve for Vp, Vs, and Vp/Vs ratio models along with seismic locations. Knowing 3D Vp/Vs (or Poisson's ratio) variations is helpful for having a more complete characterization of the mechanical properties and geological strata, in addition to Vp and Vs models. Our paper is arranged as follows: first, we provide an introduction to the field and the passive seismic monitoring program; second, we give details of the seismic tomography method employed in this study; third, we present the seismic tomography inversion details and the resulting velocity models (the model resolution analysis is included in Appendix A); finally, we discuss the tomographic images in relation to the petroleum reservoir. The application shows a great potential for using induced seismicity as a tool for reservoir imaging (3D and 4D) and velocity estimation.

MICROSEISMIC MONITORING PROGRAM

The petroleum field discussed in this paper is a large anticline created by deep-seated salt movement. The dome is about 15 × 20 km in size with a northeast-southwest axial elongation that is probably a result of regional deformation. The structure is dominated by a major central graben and two systems of faulting with two preferred directions (southeast-northwest and northeast-southwest) that affect the trapping mechanism in the oil reservoir (Figure 1). The northeast-southwest major network of faults (Fault A and Fault B) and fractures partially connects all parts of the fields together (Figure 1). The main oil production is from the Lower Cretaceous Shuaiba chalk overlain disconformably by Nahr Umr shale, while gas is produced from the shallower Natih Formation overlain by the Fiqa shale Formation. A structural cross-section of the field showing the major producing units is given by Figure 2.

To monitor the induced seismicity in the field, PDO first deployed a surface array of monitoring stations in 1999, referred to as “shallow network” by Figure 1. In 2002, another network, independent of the shallow network, was installed in the field as part of a Shell/PDO collaborative study. Unlike the surface array/shallow network, this network had borehole installations of seismic sensors at multiple levels, roughly ranging from depths 750 m – 1250 m (below the surface). The instrumentation for this network was much deeper than that of the surface network, and, therefore, this monitoring network is referred as “borehole network” in Figure 1 and in other parts of the paper. A schematic diagram of the wells and sensor positions is shown in Figure 1. The borehole network consisted of 5 closely spaced monitoring wells in the most seismically active part of the reservoir and covered a much smaller area than the surface network. However, due to sensor positions at depths, the ability to acquire data at much higher frequencies and the proximity to the two producing units (Natih gas and Shuaiba oil), the deep network recorded much smaller magnitude events than the shallow network, resulting in a greatly increased detectability of induced seismicity (roughly about 25 times more induced events per day) compared to the shallow network. The network was operational for about 18 months starting in February 2002; however, microseismic data from the last 11 months (October 2002 – August 2003) were available for this study. During that 11 month monitoring period, about 15,800 events were identified with an average rate of ~ 47/day, out of which we analyzed and located about 5,400 events (Sarkar, 2008). Attempts were made to select common events detected during this period by both (deep and shallow) networks for a joint location analysis, however, due to clock synchronization problems and difference in sensor frequency bands between the two networks, the common events could not be identified, and hence the task could not be accomplished.

SEISMIC TOMOGRAPHY METHOD

In this study, we modified a double-difference (DD) seismic tomography method developed by Zhang and Thurber (2003), also known as *tomoDD* to simultaneously solve for Vp, Vs, and Vp/Vs ratio models along with event locations. The new code is named *tomoDDPS*. DD tomography makes use of both absolute and more accurate relative arrival time data derived from event pairs observed on common stations to jointly invert for both locations and velocity models. It is a generalization of the double-difference (DD) location method of Waldhauser and Ellsworth (2000): it simultaneously solves for the three-dimensional (3-D) velocity structure and seismic event locations. DD tomography uses an evolving weighting scheme for the absolute and differential arrival times in order to determine the velocity structure progressively from larger scale to smaller scale (Zhang and Thurber, 2003). This method yields more accurate event locations and velocity structure near the source region than standard tomography, which uses only absolute arrival times (Thurber, 1983; Eberhart-Phillps, 1993; Thurber, 1993). It has the unique ability to sharpen the velocity image near the source region because of the combination of the higher accuracy of the differential time data and the concentration of the corresponding model derivatives in the source region (Wolfe, 2002). The latter results from the cancellation of model derivative terms where the ray paths from nearby earthquakes overlap away from the source region. Zhang and Thurber (2006) presented a detailed analysis of the double-difference seismic tomography method and its applications. In tomoDD, to solve the velocity structure near and outside the source region, both absolute and differential times are used but are weighted differently at different stages of inversion (Zhang and Thurber, 2003). By incorporating the absolute times into the system, it also helps stabilizing the inversion and determining the absolute seismic event locations (Zhang and Thurber, 2006). Monteiller et al. (2005) solved the double-difference tomography system using a Bayesian approach, in which only differential times are used and *a priori* event locations and velocity model are included as constraints.

The tomoDD algorithm uses P and S wave data to jointly invert for Vp, Vs, and event locations. Knowing 3D Vp/Vs variations is helpful for having a more complete characterization of the mechanical properties and geological strata. Vp/Vs variations could be determined directly from the Vp and Vs models if they have essentially identical quality. In cases where S-wave arrival data are less numerous and of poorer quality than P-wave data, however, Vs would not be as well resolved as Vp, making the interpretation of Vp/Vs variations difficult (Eberhart-Phillips, 1990). Alternatively, Vp/Vs variations can be determined by the inversion of S-P time differences (Walck, 1988; Thurber, 1993). By assuming the ray paths of P and S waves are identical, which is true when Vp/Vs is constant, Vp/Vs can be determined from S-P arrival times $\mathrm{Ts} - \mathrm{Tp}$, as follows (Thurber, 1993),

$$\mathrm{T}s - \mathrm{T}\mathrm{p} = \int_{path} \left(\frac{\mathrm{V_p}}{\mathrm{V_s}} - 1 \right) \frac{\mathrm{ds}}{\mathrm{V_p}} \tag{1}$$

where Ts and Tp are S and P wave arrival times at one station, respectively. Since P and S waves from the same event share the same origin time, the unknown origin times are removed from this equation.

However, in case of a complicated geological area, the P and S ray paths may differ significantly and thus the results may be biased when equation (1) is applied to them. To reduce the effect of the assumption of similar ray paths for P and S waves, two strategies are implemented in our inversion algorithm. (1) At each iteration, ray paths for P and S waves are checked based on the Hausdorff distance defined as the "maximum distance of a set to the nearest point in the other set" (Rote, 1991). They are subsequently removed from the Vp/Vs inversion if they are considerably different. (2) Differential S-P times from event pairs at common stations are used in the same way as DD tomography to determine Vp/Vs ratios. For strategy (1), the ray paths are calculated based on the velocity models determined directly using P- and S-wave data. We do not obtain the Vs model using Vp values and Vp/Vs ratios since this method may result in biased Vs values (Wagner *et al.*, 2005). We generally require that the Hausdorff distance between P and S ray paths be smaller than 5% of the average length of P and S ray paths. For strategy (2), by using the differential S-P times, we can remove the effect of different ray paths of P and S waves outside the source region. Near the source region, P- and S-wave ray paths are generally closer to each other.

Based on equation (1), the differential S-P arrival time residuals from event *i* to station *k* can be linearly related to the perturbations of event locations and Vp/Vs ratios, as follows:

$$dr_{k\,SP}^{i} = (T_{kS}^{i} - T_{kP}^{i})^{obs} - (T_{kS}^{i} - T_{kP}^{i})^{cal} = \sum_{l=1}^{3} \frac{\partial T_{kS}^{i}}{\partial x_{l}^{i}} \Delta x_{l}^{i} - \sum_{l=1}^{3} \frac{\partial T_{kP}^{i}}{\partial x_{l}^{i}} \Delta x_{l}^{i} + \int_{i}^{k} \delta(Vp/Vs)\, {ds}/{Vp} \qquad (2)$$

where $(Ts\text{-}Tp)^{cal}$ is the calculated differential time between the S and P wave arrival time at a given station, $(Ts\text{-}Tp)^{obs}$ is the observed differential time, $\delta(Vp/Vs)$ is the perturbation to Vp/Vs, and ds is an element of path length. Similar to the equations of DD tomography, we subtract a similar equation for event j observed at station k from equation (2), as follows,

$$\begin{aligned} dr_{k\ SP}^{i,j} = dr_{k\,SP}^{i} - dr_{k\,SP}^{j} &= \sum_{l=1}^{3} \left(\frac{\partial T_{kS}^{i}}{\partial x_l} - \frac{\partial T_{kP}^{i}}{\partial x_l} \right) \Delta x_l^{i} - \sum_{l=1}^{3} \left(\frac{\partial T_{kS}^{j}}{\partial x_l} - \frac{\partial T_{kP}^{j}}{\partial x_l} \right) \Delta x_l^{j} \\ &\quad + \int_{i}^{k} \delta(Vp/Vs) \, {}^{ds}\!/_{Vp} - \int_{j}^{k} \delta(Vp/Vs) \, {}^{ds}\!/_{Vp} \end{aligned} \tag{3}$$

where

$$\begin{aligned} dr_{k\ SP}^{i,j} &= (T_{kS}^{i} - T_{kP}^{i})^{obs} - (T_{kS}^{i} - T_{kP}^{i})^{cal} - (T_{kS}^{j} - T_{kP}^{j})^{obs} + (T_{kS}^{j} - T_{kP}^{j})^{cal} \\ &= (T_{kS}^{i} - T_{kS}^{j})^{obs} - (T_{kP}^{i} - T_{kP}^{j})^{obs} - (T_{kS}^{i} - T_{kS}^{j})^{cal} + (T_{kP}^{i} - T_{kP}^{j})^{cal} \end{aligned} \tag{4}$$

Equation (3) shows that the Vp/Vs structure can be directly imaged by using the differential P and S arrival times. More accurate differential times can be calculated from waveform cross-correlation techniques for similar waveforms and/or absolute catalog data.

In our seismic tomography, we combined the DD tomography equations for P- and S-wave data and equations (2) and (3) for absolute and differential S-P data to solve for event locations, Vp, Vs, and Vp/Vs models, starting from a constant Vp/Vs model. Similar to the smoothing constraints applied to velocity changes during the inversion (Zhang and Thurber, 2003), we also apply the smoothing constraints to the perturbations of Vp/Vs during each step of joint inversion. The smoothing weights applied to the perturbations of Vp/Vs are smaller than the weights for Vp and Vs changes due to the smaller scale of Vp/Vs values and relatively smaller amount of S-P data. The relative weightings between the different data types (absolute catalog data, differential catalog data, and waveform cross-correlation data, respectively) are the same as DD tomography (Zhang and Thurber, 2003). S-P data are assigned the same weight as the corresponding S-wave data. The new algorithm is able to produce more accurate event locations, Vp, Vs and Vp/Vs models due to the usage of more accurate differential times and the reduced effect of different ray paths for P and S waves.

DATA AND ANALYSIS

For the borehole microseismic monitoring study, we had field data from October 2002 – August 2003. During that period, about 15,800 events had been identified with an average rate of ~ 47/day. The typical frequency content for events close to the monitoring wells was in the range 100 to 300 Hz, while the more distant large events typically had peak frequency between 20 and 40 Hz. Figure 3 shows an example of three components from an induced event recorded by a deep-network sensor with a sampling rate of 0.5 milliseconds (ms). About 5,400 events were successfully located using a probabilistic, advanced grid-search location method known as NonLinLoc (Lomax et al., 2000). A detailed account of event location analysis and their correlations with faults and fractures are given by Sarkar (2008). Figure 4 shows the epicenter and depth distribution of all the located events. Most of the seismic events lie along the two major NE-SW faults (Fault A and Fault B) in the field. Seismicity is more continuous along Fault A than along Fault B. It was also noticed that many events did not occur along the two major faults, indicating some significant amount of "in-fill" faulting/fracturing occurred during the production in the reservoir. During the 11 month interval, the events were observed to have been spread between 500 and 1500 m depth (relative to the MSL).

Out of ~ 5,400 events analyzed and located for reservoir monitoring with the borehole network during Oct 2002 – August 2003, we selected 1999 microseismic events for reservoir imaging using the double-difference tomography method. All the selected events had at least 12 P and/or S arrival time picks so that they could be reliably relocated. The selected event distribution (epicenters and depths from the NonLinLoc location algorithm), and the borehole network stations are shown in Figure 5. Most of the ray paths (not shown) from the induced events to the deep network stations provide good coverage to do seismic tomography using these data. Among the selected 1999 events there were about 25000 P arrivals and about 11800 S arrivals recorded by 32 borehole stations. From them ~11800 S-P times were derived. We also constructed ~143000 differential P times and ~49000 differential S times from event pairs with an average offset of 180 m. The minimum offset between event pairs is 50 m and the maximum offset is 1.5 km. Each event has at most 15 pairs with other events. From the differential P and S times, ~49000 differential S-P times were constructed. Cross-correlation times for the deep network data were not available at the time of study. As for the coordinate system used in the inversion, a Cartesian system was set up with the positive Y axis oriented 50^o clockwise from north (roughly parallel to the strike of the major faults), and the X axis oriented positive southeast (Figure 5). We use a series of regular grid nodes in three dimensions to represent the velocity model. The velocity values are specified on grid nodes and for regions between nodes they are interpolated from neighboring nodes using a linear interpolation method. The inversion grid nodes (in this *rotated* coordinate system) are located at X = -1.1, -0.6, -0.3, 0, 0.3, 0.6 and 1.0 km, Y = -2.5, -1.5, -1.0, -0.5, 0, 0.8, 1.5, and 2.5 km, and at Z = 0, 0.50, 0.60, 0.70, 0.80, 0.90, 1.10, 1.20, 1.30, 1.60, 1.80, 1.90, 2.00, and 2.20 km. In total there are 784 inversion grid nodes. The starting Vp model for tomography inversion is a layered model derived from averaging 5 well-logs (Sonic) at 5 nearby wells (Figure 6). For the starting Vp/Vs ratio a constant value of 1.92 is used, which was obtained from the check-shot survey and was also confirmed from the Wadati diagram (Sze, 2005). Different starting Vp/Vs rations such as 1.732 and 1.8 were also tested and the resulting Vp/Vs models are comparable. Smoothing and damping values were chosen via a trade-off analysis of model variance and data variance so that the selected values reduce most of the data variance without causing large increases in the model variance (Figure 7). The ART-PB ray tracing algorithm of Um and Thurber (1987) is used to calculate ray paths and travel times from seismic events to stations. The calculated travel times are accurate at 0.5 ms. The LSQR method of Paige and Sanders (1982) is used to solve the complete tomographic system. The initial root-mean-square (RMS) residual was 27 ms and the final RMS residual was 17 ms.

To check the model resolution, we used both the conventional checkerboard test (Humphreys and Clayton, 1988) and the strict resolution test based on the resolution matrix (Aster et al., 2005). For the checkerboard test, we added ±5% velocity anomalies to every other grid node in the X and Y directions and to every other two grid nodes in the Z-direction to the final model. As seen from Figure A1, the model resolution is reasonably good in the middle part of the model. In addition to the checkerboard test, we also built the resolution matrix of the inverse problem using a new version of the tomoDD code that incorporates the PROPACK package to estimate the model resolution matrix for large seismic tomography problems (Zhang and Thurber, 2007). The details of model resolution analysis are included in Appendix A. We also compared the velocity models from the double-difference tomography method to those using only the absolute times (conventional seismic tomography) in Appendix B. The comparison showed that the double-difference tomography method is able to resolve more detailed velocity structure near the source region.

In the current version of the tomoDDPS code, because the LSQR algorithm is used to solve the complete tomographic system, it lacks the ability to strictly analyze the location uncertainty. Therefore we just qualitatively compare the relocated event locations to initial event locations. Compared to initial event locations, their relocations from the tomoDDPS algorithm are slightly improved (Figure 8). For example, we see tighter clustering of the events along the fault A at depths and sharper delineation and better identification of the feature on the southwestern side of the fault B. However, the location improvement is modest due to the lack of waveform cross-correlation data at the time of study. We also calculated RMS residual for the individual event. Figure 9 shows the histogram of the RMS residuals for all the events. The average RMS residual for the individual event is 4.3 ms and the maximum is 16 ms. This indicates that the average event mislocation error would be on the order of 20 m if we take the average Vp of 4 km/s for the region.

RESULTS AND DISCUSSIONS

In this section we show and discuss velocity models of the reservoir derived from the application of the new tomoDD algorithm to the induced seismicity data. We show map view slices and depth cross-sections of the three-dimensional Vp, Vs and Vp/Vs models by Figures 10 and 11, respectively. The relocated events are also projected onto respective map view slices and cross sections. The absolute velocity plots instead of velocity perturbations were used to better identify various layers in the reservoir and compare the variation of velocities between layers and across faults.

The model resolution analysis based on the checkerboard test and the resolution matrix shows that the velocity models between depths 0.7 km and 1.1 km are relatively well resolved (see Appendix A). From the map view of the velocity models, we see substantial variations in Vp, Vs, and Vp/Vs models (Figure 10). Compared to the starting velocity model derived from the sonic logs, we also see substantial deviations. We note that the wells used for deriving the starting model are located outside the model region with a complicated faulting regime (Figure 1). Therefore it is possible the velocity changes abruptly. It could also be partly due to the fact that the reservoir layers are not flat but dipped or domed and the horizontal grid could cut across some formations. There exists a clear velocity contrast across the NE-SW fault A (Figure 10). Along the strike of fault A, the velocity contrast pattern changes. For example, in the depth slices of 0.7 and 0.8 km, the fault can be divided into three segments (Figure 10). For the fault segment between Y=2.5 and ~1.5 km, the velocity is lower to the west and higher to the east. For the middle fault segment between Y=~1.5 and Y=-0.5 km, the velocity is higher to the west and lower to the east. Between Y=-0.5 km and -2.5 km, the velocity is lower to the west and higher to the east of the fault. The two transition points at Y=1.5 km and Y=-0.5 km correspond well to the mapped conjugate fault traces with a major strike of northwest-southeast (Figure 5a). The same pattern is less evident for the depth slice of 0.9 km but it is still visible. For the depth slice of 1.1 km, the velocity contrast only exists to the northeast of Y=~1.0 km. However, these observations may well be due to the degraded model resolution for these two depth slices. The induced microearthquakes associated with fault A are mainly located along the middle segment of the fault. For the NE-SW fault B, the mapped fault trace is not continuous and breaks at around Y=0.8 km and Y=-1 km (Figure 5). The velocity contrast is also clear across the mapped southeastern fault trace with velocity higher to the northwest (Figure 10). In the map view, a relatively high-velocity body exits down to the depth 0.9 km between Y=0.8 and -1 km, where the fault trace discontinues (indicated by yellow circles in Figure 10).

In the across-fault northwest-southeast cross sections (Figure 11), we mostly see a layered structure similar to the starting model derived from an average of a few sonic well-logs from the field (Figures 6). However, a substantial lateral variation in both Vp and Vs models exists in some cross sections (Figure 11). For example, in the cross sections of Y=0 and -0.5 km, a bowl-shaped low-velocity anomaly exists at depths between 0.8 and 1 km, which may be related to the displacement of the Natih formation. To the southeast edge of this bowl-shaped low velocity anomaly, there is a cloud of seismicity, which is also associated with the relatively high-velocity body identified on the depth slices of 0.7, 0.8 and 0.9 km as indicated by yellow circles in Figure 10.

We started the inversion from a constant Vp/Vs ratio of 1.92. Between depths 0.7 km and ~1.1 km, the resolution for the Vp/Vs ratio model is relatively good, comparable to the Vs model resolution. In general, the Vp/Vs ratio is low (<1.75) in the shallower part and large (>1.75) in the deeper part of the model (Figure 11). The depth range of the low Vp/Vs ratio is consistent with that of gas producing reservoir Natih A formation (Figure 2). Similar estimates for Vp/Vs ratio have also been obtained from sonic-Vp and Vs measurements from well-logs. The low Vp/Vs ratios could be due to the combined effect of lithology and gas content. As shown by the laboratory study, high gas content can cause the reduction in Vp, Vs and Vp/Vs ratio (Mavko et al., 2003). The high Vp/Vs ratio in the regions with a reasonably good resolution between 0.7 and 1.2 km is likely caused by the fluid saturated formation. We also see horizontal variations in the Vp/Vs ratio model (Figure 10). In the cross sections of Y=-2.5 and -1.5 km, the southeastern fault seems to separate two Vp/Vs anomaly zones with low Vp/Vs to northwest and high Vp/Vs to southeast (Figure 11). For the cross-sections of Y=-1 to 0 km where the southeastern fault trace breaks, the induced earthquakes are scattered and clouded and the Vp/Vs ratios are low, indicating high gas content in this area (indicated by yellow circles in Figure 11). Actually, a gas producing well exists in this area. This cloud of seismicity may therefore be related to stress perturbation due to gas production, in which existing fractures may have been reactivated and new fractures may have been induced.

The distribution of induced seismicity shows different characteristics for the two NE-SW striking faults A and B. In the cross-sections of Y=-2.5 and -1.5 km, the induced microseismic events associated with the fault B are mainly confined to the fault zone and penetrate as deep as 1.4 km. In comparison, between the cross-sections of Y=-0.5 km and 0 km, the events are mostly confined to depths shallower than 0.9 km and located above a high-velocity body. They are not concentrated but are scattered to the southeastern side of the fault. However, the induced events associated with fault A are mainly concentrated around the fault zone and located down to the depth of 1.1 km. This indicates that the induced microseismic events are mainly located in the weak zones such as fault zones. The induced seismicity was mainly located in and around the gas formation; therefore the primary cause of induced seismicity in the field is attributed to the compaction of the Natih gas formation.

Seismic imaging of hydrocarbon reservoirs using passively induced seismicity data is not very common in the oil and gas industry. In fact, the application of reservoir-scale passive seismic tomography at a producing petroleum field described in this study is probably the first of its kind. The results obtained from this study show much promise for further development and application of this technology. The challenges faced and lessons learned in this study will be very useful in making advances in this new type of reservoir imaging technique.

To achieve more accurate velocity images from the passive seismic tomography, we may improve the tomography method applied in this study. For example, adaptive/non-uniform gridding technique to adequately model the shape of the layer boundaries needs to be incorporated (Zhang and Thurber, 2005). Finer grid spacing and some additional regularization scheme based on *a priori* geologic information could also be useful in improving the inversion results. Another major application of induced seismicity tomography would be to interpret the structural and velocity changes with time. If passive seismic monitoring is carried out long enough in a field and data such as that described in this study (deep-borehole network) can be acquired over a significant portion of the reservoir, there is a potential to carry out time-lapse (4-D) seismic tomography using induced seismicity data (e.g. Patane et al., 2006).

CONCLUSIONS

A new version of the double-difference seismic tomography method was developed to simultaneously solve for the event locations, Vp, Vs and Vp/Vs models by directly using S-P times in addition to the P and S arrival times. We have applied the new method to the induced seismicity data recorded by a borehole network at a producing petroleum field in Oman. The event locations showed strong correlation with the existing fault traces. In this producing petroleum field in Oman, the majority of the seismic events are likely caused by reactivation of existing faults due to compaction of the gas bearing formation in response to declining reservoir pressure.

Reservoir imaging shows encouraging results in identifying structures and velocity changes within reservoir layers. Clear velocity contrast was seen across the two major NE-SW faults A and B. Considerable velocity variations also exist along the strike of the two NE-SW faults. The transition points along the strike seem to be consistent with the intersection points with another conjugate NW-SE fault system. There exists a bowl-shaped low-velocity anomaly within the two NE-SW faults, probably caused by the displacement of gas formation. The Vp/Vs ratios are smaller than 1.75 in the shallower part of the model, consistent with the depth range of the upper gas producing reservoir, whereas they are greater than 1.75 in the deeper part of the model. This study indicates that the three-dimensional seismic tomography using the induced seismicity data has a great potential for reservoir imaging and property estimation.

Induced seismicity occurs during the life time of the reservoir. In this study, we had data for a period of only 10 months. We were able to obtain reservoir properties at one snapshot in time. If data were available for longer periods, the tomography could be repeated over a sequence of time intervals. This would make it possible to determine changes in the reservoir properties. In essence, this would be "time lapse" monitoring of the reservoir and its fluids.

ACKNOWLEDGEMENTS

We would like to thank the Petroleum Development Oman for the data and the support of this project. We also appreciate constructive reviews from the Associate Editor Tamas Nemeth and three reviewers.

Appendix A – Model Resolution Analysis

To check the model resolution, we used both the conventional checkerboard test (Humphreys and Clayton, 1988) and the strict resolution test based on the resolution matrix (Aster et al., 2005). The X and Y coordinates of the plots used to show the model resolution test results are of the rotated coordinate system shown in Figure 5 (a).

A1 Checkerboard Test

To create a checkerboard model, we added ±5% velocity anomalies to every other grid node in the X and Y directions and to every other two grid nodes in the Z-direction of the final velocity models. Synthetic travel time data (absolute and differential) were generated for this checkerboard velocity model using the same source-receiver geometry as the real data, which were subsequently inverted using the double-difference tomography method. As for the starting model for this "synthetic" inversion, we used the same initial model (shown by Figure 6) to be used for the “real” inversion and also the same regularization parameters. In Figure A1 we plotted the inverted model perturbations at different depths for the P-wave velocity. On the inverted models, we also superimposed the derivative weigh sum (DWS) contours (plotted in blue and labeled in red). The DWS is a statistical parameter that helps the assessment of parameter resolution; it gives a measure of density of rays that pass near a grid point that is weighted according to how close each ray passes to the node (Toomey and Foulger, 1989). It is, therefore, superior to the more commonly quoted “hit” matrix, which is merely a count of the number of rays that pass close to the grid point. A large DWS indicates that the velocity at the grid point is based on a large body of data. However, like the ray hit-count, the DWS also does not take into account the ray direction. The checkerboard test results help us examine where in the reservoir and how well the double-difference tomography method is likely to resolve the *actual* model. As seen by the plots of Figure A1, the best resolution is obtained between depths of 0.7 – 1.1 km. On each plane, the DWS contour distributions indicate that the central part (high DWS) is much better resolved than the edges (low DWS) of the model. At or below Z = 1.2 km and at or above Z = 0.6 km (not shown), the checkerboard recovery is very poor; therefore the actual inversion results at those depths should not be depended upon. The model parameters by the actual inversion, more or less, should be well resolved in the central part of the selected tomography region and between depths 0.7 – 1.1 km, according to the checkerboard test.

A2 Resolution Matrix

In addition to doing the routine checkerboard test, we also computed the resolution matrix of the inverse problem using a new version of the double-difference tomography code that incorporates the Partial Reorthogonalization Package (PROPACK) developed by Larsen (1998) to estimate the model resolution matrix for large seismic tomography problems (Zhang and Thurber, 2007).

We showed the diagonal resolution values of the resolution matrix for Vp and Vs in both depth slices (Figure A2) and the across-fault cross sections (Figure A3). We consider a region to be adequately resolved where diagonal elements of the resolution matrix are greater than 0.25 (Thurber *et al.*, 2003). The higher the diagonal resolution value, the more likely the model is resolved. In the depth slices at 0.7, 0.8, 0.9 and 1.1 km, the resolution is reasonably well for most part of the model, especially between the two NE-SW faults (between X = -0.5 and X =0.5). As expected the resolution is poor near the edges of the model. For the depth slices above 0.5 km and below 1.1 km, the resolution is poor in most parts.

We see almost no resolution between 1.2 km and 1.3 km, as identified by a sharp break of the resolution contour above and below those depths (Figure A3). This is due to the presence of a low velocity layer at that depth. As seen from the initial velocity model (Figure 6), a large velocity contrast between adjacent nodes (e.g. from Z=1.3 to Z=1.6 km, Vp changes from 3 km/s to 5 km/s, which is a 67% increase), forces the ray paths from events at that depth to travel along the layer boundary of the adjacent layer (above or below, depending on where the event is in that layer and its position relative to the station), thereby yielding very poor ray coverage in that layer. Such large contrasts are “problems” for the tomographic imaging; however such is the reality in sedimentary layers (as seen by the well-log on Figure 6) – which makes detailed imaging of petroleum reservoirs using induced events a very challenging problem. The patterns of resolution contours for Vs are very similar to those for Vp, except that at the same regions Vs is less well resolved than Vp. This is also expected because S-picks are much fewer in number and assigned lower weights than P-picks.

Therefore, it may be observed that the checkerboard test results (Figure A1) and the resolution test results (Figures A2 and A3) are consistent. To summarize both test results: for the given event and station distribution (for the deep-borehole network), and the background velocity model, reservoir images that are obtained by using the double-difference tomography method would be most reliable between 0.6 and 1.1 km depths, and in the region between the two faults and bounded by the stations.

Appendix B – Comparison of velocity models from the double-difference and conventional seismic tomography methods

We compared the velocity models from the double-difference and conventional seismic tomography methods. For the conventional seismic tomography, the same *tomoDDPS* code is adopted but only absolute times are used. For a fair comparison, we also recalculated optimal smooth weighting and damping parameters for the conventional seismic tomography through a trade-off analysis of model variance and data variance. The optimum smooth weighting parameter for conventional seismic tomography is about half of that for double-difference tomography. Figure A4 shows comparison of Vp models at different depths from the two methods. The event locations from the two methods are also projected to different depth slices, respectively. The event locations from double-difference tomography show better alignment along fault traces and more linear structures (Figure A4). The diagonal resolution matrix values are also plotted in white contours. For double-difference tomography, resolution matrix is calculated for the later stage of inversion where the differential times are weighted 20 times higher than the absolute times. In general, for the regions around the seismicity, the resolution values for double-difference tomography are higher. The comparison shows considerable differences in two velocity models. In general, the double-difference tomography Vp model shows a more clear contrast across the fault and seismic events are more likely distributed along the velocity contrast or around relatively high velocity bodies, as indicated by white circles in Figure A4. The comparison indicates that the double-difference seismic tomography method is able to resolve more detailed structures around seismicity.

REFERENCES

Aster, R. C., B. Borchers, and C. H. Thurber, 2005, Parameter estimation and inverse problems, Elsevier Academic Press, Burlington, MA.

Deflandre, J.P., J. Laurent, D. Michon, and E. Blondin, 1995, Microseismic surveying and repeated VSPs for monitoring an underground gas storage reservoir using permanent geophones, First Break, **13**, pp. 129–138.

Eberhart-Phillips, D., 1990, Three-dimensional P and S velocity structure in the Coalinga region, California, Journal of Geophysical Research, **95**, 15343-15363.

Eberhart-Phillips, D., 1993, Local earthquake tomography: earthquake source regions, *in* H.M. Iyer and Irahara, eds., Seismic Tomography: Theory and Practice, Chapman and Hall, New York, 613–643.

Grasso, J., 1992, Mechanics of seismic instabilities induced by the recovery of hydrocarbons, Pure and Applied Geophysics, **139**, 507–534.

Humphreys, E., and R. W. Clayton, 1988, Adaptation of back projection tomography to seismic travel time problems, Journal of Geophysical Research, **93**, 1073–1085.

Keck, R. G., and R. J. Withers, 1994, A field demonstration of hydraulic fracturing for solids waste injection with real-time passive seismic monitoring, Proceedings of the SPE 69th Annual Technical Conference and Exhibition, SPE 28495, New Orleans, LA.

Kristansen, T.G., O. Barkved, and P.D. Pattilo, 2000, The use of passive seismic monitoring in well and casing design in the compacting and subsiding Valhall Field, North. SPE Paper 65134.

Larsen, R. M., 1998, Lanczos bidiagonalization with partial reorthogonalization, Department of Computer Science, Aarhus University, Technical Report, DAIMI PB-357, September 1998.

Lomax, A., J. Virieux, P. Volant and C. Berge, 2000, Probabilistic earthquake location in 3D and layered models: Introduction of a Metropolis-Gibbs method and comparison with linear locations, *in* C.H. Thurber, and N. Rabinowitz, eds., Advances in Seismic Event Location, Kluwer, Amsterdam, 101-134.

Mavko, G., T. Mukerji, and J. Dvorkin, 2003, The Rock Physics Handbook: Tools for Seismic Analysis of Porous Media, Cambridge University Press, 340 pp.

Maxwell, S.C., R.P. Young, R. Bossu, A. Jupe, and J. Dangerfield, 1998, Microseismic logging of the Ekofisk reservoir, paper SPE 47276, Proceedings of the 1998 SPE/ISRM Eurock '98, Trondhiem, Norway.

Maxwell, S.C., J. Du, and J. Shemeta, 2008, Passive seismic and surface monitoring of geomechanical deformation associated with steam injection, The Leading Edge, **17**, 1176-1184.

McGillivray, P.R., 2004, Microseismic and Time-lapse Monitoring of a Heavy Oil Extraction Process at Peace River, 73rd SEG Annual Conference, Denver, CO.

Monteiller V., J.-L. Got, J. Virieux, P. Okubo, 2005, An efficient algorithm for double-difference tomography and location in heterogeneous media, with an application to the Kilauea volcano, J. Geophys. Res., **110**, B12306, doi:10.1029/2004JB003466.

Paige, C.C., and M.A. Saunders, 1982, LSQR: an algorithm for sparse linear equations and sparse least squares, ACM Transactions on Mathematical Software, **8**, 43-71.

Patane, D., G. Barberi, O.Cocina, P. De Gori, and C. Chiarabba, 2006, Time-resolved seismic tomography detects magma intrusions at Mount Etna, Science, **313**, 821-823.

Rote, G., 1991, Computing the minimum Hausdorff distance between two point sets on a line under translation, Information Processing Letters, **38**, 123-127.

Rutledge, J. T., and W.S. Phillips, 2003, Hydraulic stimulation of natural fractures as revealed by induced microearthquakes, Carthage Cotton Valley gas field, East Texas, Geophysics, **68**, 441–452.

Rutledge, J.T., W.S. Phillips, and B.K. Schuessler, 1998, Reservoir characterization using oil-production-induced microseismicity, Clinton county, Kentucky, Tectonophysics, **289**, 129–152.

Sarkar, S., 2008, Reservoir Monitoring Using Induced Seismicity at a Petroleum Field in Oman, Ph.D. Thesis, Massachusetts Institute of Technology, Cambridge, MA.

Sze, E. K-M., 2005, Induced seismicity analysis for reservoir characterization at a petroleum field in Oman, Ph.D. Thesis, Massachusetts Institute of Technology, Cambridge, MA.

Thurber, C. H., 1983, Earthquake locations and three-dimensional crustal structure in the Coyote Lake area, central California, Journal of Geophysical Research, **88**, 8226–8236.

Thurber, C. H., 1993, Local earthquake tomography velocities and Vp/Vs—theory, *in* H.M. Iyer ,and K. Hirahara, eds., Seismic Tomography: Theory and Practice, Chapman & Hall, London, 20, 563–580.

Toomey, D. R., and G. R. Foulger, 1989, Tomographic inversion of local earthquake data from the Hengill–Grensdalur central volcano complex, Iceland, Journal of Geophysical Research, **94**, 17497–17510.

Um, J., and C.H. Thurber, 1987, A fast algorithm for two-point seismic ray tracing, Bulletin of Seismological Society of America, **77**, 972-986.

Wagner L. S., S. Beck, and G. Zandt, 2005, Upper mantle structure in the south central Chilean subduction zone (30° to 36°S), Journal of Geophysical Research, **110**, B01308, doi:10.1029/2004JB003238.

Walck, M. C., 1988, Three-dimensional Vp/Vs variations for the Coso region, California. Journal of Geophysical Research, **93**, 2047–2052.

Waldhauser, F., and W. L. Ellsworth, 2000, A double-difference earthquake location algorithm: Method and application to the northern Hayward fault, Bulletin of the Seismological Society of America, **90**, 1353-1368.

Wilson, S., R. Jones, W. Wason, D. Raymer, and P. Jaques, 2004, Passive seismic makes sense for 4D reservoir monitoring, First Break, **23**, 59-65.

Wolfe, C. J., 2002, On the mathematics of using difference operators to relocate earthquakes, Bulletin of the Seismological Society of America, **92**, 2879-2892.

Zhang, H., and C. H. Thurber, 2007, Estimating the model resolution matrix for large-seismic tomography problems based on Lanczos bidiagonalization with partial reorthogonalization, Geophysical Journal International, **170**, 337–345.

Zhang, H., and C. Thurber, 2006, Development and applications of double-difference seismic tomography, Pure and Applied Geophysics, **163**, 373-403.

Zhang, H. and C.H. Thuber, 2005, Adaptive-mesh seismic tomography based on tetrahedral and Voronoi diagrams: Application to Parkfield, California, Journal of Geophysical Research, **110**, B04303, doi:10.1029/2004JB003186.

Zhang, H., and C. H. Thurber, 2003, Double-Difference Tomography: The Method and Its Application to the Hayward Fault, California, Bulletin of the Seismological Society of America, **93,** 1875-1889.

FIGURE CAPTIONS

Figure 1. Combined plot of both borehole and shallow networks used for passive seismic monitoring at the field. Well positions of the shallow network are shown in green (sensor positions are indicated by squares). Well positions for the 5 monitoring wells of the borehole network are shown by 5 different colors, with triangles denoting sensor positions in each well at different depth levels. Red dots show well locations with sonic logs available for deriving the 1D model in Figure 2. Red thin lines indicate faults mapped from surface seismic. Also plotted are two major horizons – Natih A in red, and Shuaiba in blue. Zero of the depth axis indicate mean sea level (MSL), which is roughly 110 m below the surface. Northing and Easting values correspond to a relative Cartesian coordinate system derived specifically for this study.

Figure 2. Structural cross-section of the field, with labels of various geologic units. Gas is produced from the uppermost green layer (Natih A) and underneath that is the oil producing layer Shuaiba shown in red. The fault lines in brown are suggested extension of the two major faults. Also shown on top with symbols are locations of some of the oil production and water injection wells that have completion depths into and below Shuaiba. The vertical axis shows depths in meters relative to the Mean Sea Level. (Figure courtesy: PDO)

Figure 3. Three components of seismic waveform from an induced event detected by the borehole network, along with the P and S-phase picks.

Figure 4. Location of induced seismic events occurring every other day during the period Oct 2002 – Aug 2003. Top: Showing event epicenters (blue dots), with fault maps derived from surface seismic at Natih horizon (black lines) and surface coordinates of the monitoring wells (red triangles). Bottom: Showing depth distribution of the events along a vertical plane (East-

West section). The length of the West to East axis shown on this plot is 9 km (corresponding to a profile line extending from 2 to 11 km along the Easting axis of the top plot).

Figure 5. (a) Setup for double-difference tomography using borehole network data in map view: events (grey dots), stations (triangles), inversion grids (blue "+" symbols), and the center of the rotated coordinate system (red circle). Also shown are faults mapped from surface seismic in black lines, and a schematic diagram of the rotated coordinated system on the right. (b) Depths of events (grey dots) shown along strike (NE-SW) and normal to the major strike (NW-SE) direction. Event locations are derived from the NonLinLoc location algorithm.

Figure 6. Initial P-wave velocity model for depth nodes shown by yellow squares. For travel time calculation, the velocity between two nodes is linearly interpolated – as shown by the red curves. Blue curve shows an average Vp derived from five Sonic logs, which serves as a guideline for selecting the depth nodes for inversion and the corresponding starting velocities.

Figure 7. Trade-off analysis of data variance and model variance for a series of damping values from 13 to 93 and smooth weighting values of 0.5 to 5. (a) Trade-off curves for different smooth weighting values. (b) Trade-off curves for different damping values. The selected smooth weighting and damping values are 1.5 and 35.

Figure 8. Comparison of initial (blue dots) and double-difference tomography relocations (red dots) of induced events used for reservoir imaging. Event locations are plotted for the rotated coordinate system (as shown by Figure 5). On the epicenter map, black lines and green triangles show existing faults and locations of monitoring wells (boreholes), respectively.

Figure 9. Histogram of RMS travel time residuals for events based on final velocity models and event locations from double-difference tomography.

Figure 10. Horizontal slices of the three-dimensional Vp, Vs, and Vp/Vs models (column-wise, from left to right) at different depths. Included in the plots are preexisting fault maps derived at Natih horizon from surface seismic (grey lines), induced seismicity locations for ± 100 m depth of each section plot (black dots), and the resolution contours obtained from the resolution matrix test (white). As per the resolution matrix test, only the regions that have resolution values > 0.3 are considered for interpretation.

Figure 11. Across-fault cross sections of Vp, Vs, and Vp/Vs (column-wise, from left to right) at different Y locations. Also shown on the plots in black are the contour lines and labels of the variables. Induced seismicity locations (black dots) within ± 500 m of each section are superimposed on the velocity images. Also, the diagonal resolution contours obtained from the resolution matrix are superimposed in white. On each of these images, regions where the resolution values are greater than 0.3 can be used for interpretation.

Figure A1. Inverted checkerboard patterns at different depths. DWS contours from inversion are plotted in blue and labeled in red.

Figure A2. Diagonal resolution contours for Vp and Vs models at different depths.

Figure A3. Diagonal resolution contours for the across-fault cross sections. The model is likely to be resolved in places where the contour is greater than 0.3.

Figure A4. Comparison of Vp models at depths 0.7, 0.8 and 0.9 km from DD tomography and conventional tomography. (Left) DD tomography Vp models and event locations; (Middle) Conventional tomography Vp models and event locations; (Right) Vp differences with event locations from DD tomography.

FIGURES

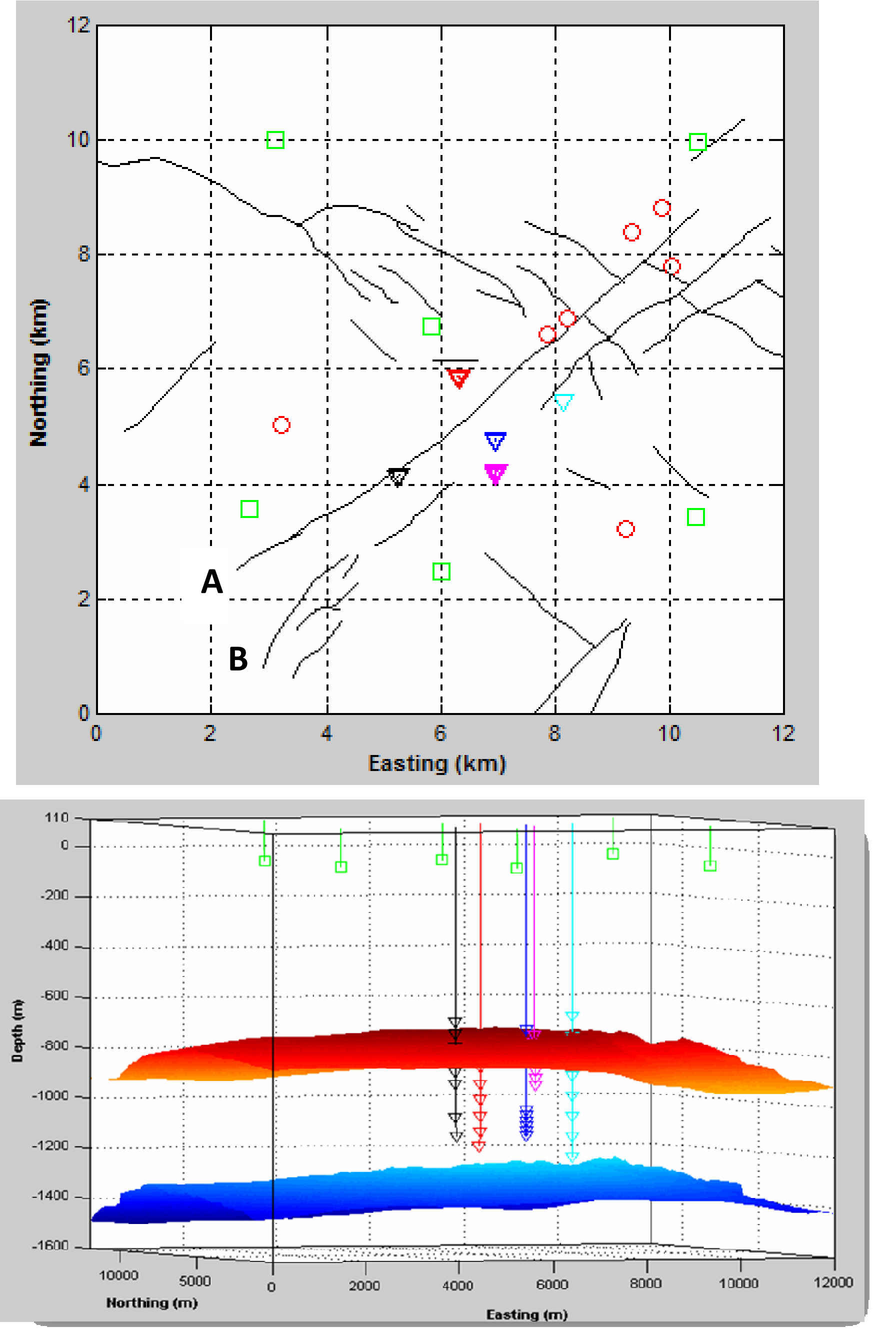

Figure 1: Combined plot of both shallow and borehole networks used for passive seismic monitoring at the field. Well positions of the shallow network are shown in green (sensor positions are indicated by squares). Well positions for the 5 monitoring wells of the borehole network are shown by 5 different colors, with triangles denoting sensor positions in each well at different depth levels. Red dots show well locations with sonic logs available for deriving the 1D model in Figure 2. Red thin lines indicate existing faults and two major NE-SW faults are labeled as A and B. Also plotted are two major horizons – Natih A in red, and Shuaiba in blue. Zero of the depth axis indicate mean sea level (MSL), which is roughly 110 m below the surface. .

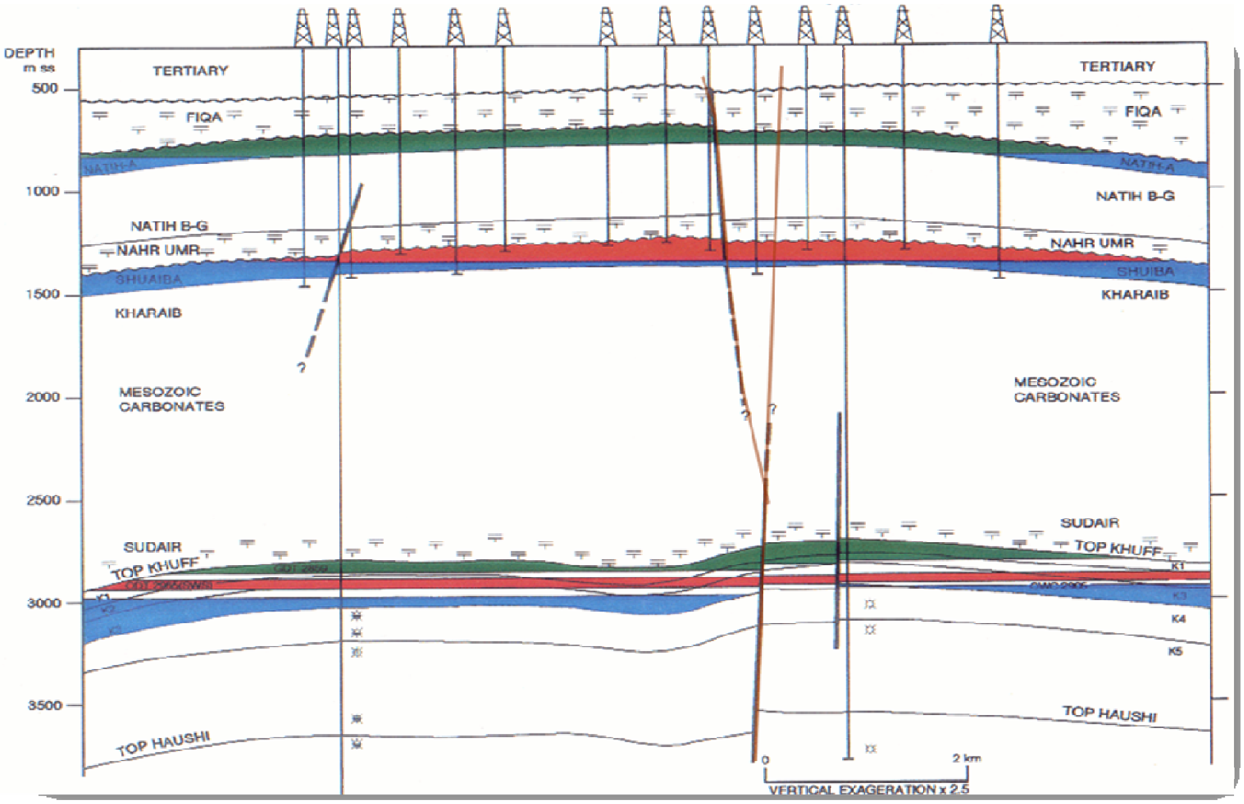

Figure 2. Structural cross-section of the field, with labels of various geologic units. Gas is produced from the uppermost green layer (Natih A) and underneath that is the oil producing layer Shuaiba shown in red. The fault lines in brown are suggested extension of the two major faults. Also shown on top with symbols are locations of some of the oil production and water injection wells that have completion depths into and below Shuaiba. The vertical axis shows depths in meters relative to the Mean Sea Level. (Figure courtesy: PDO)

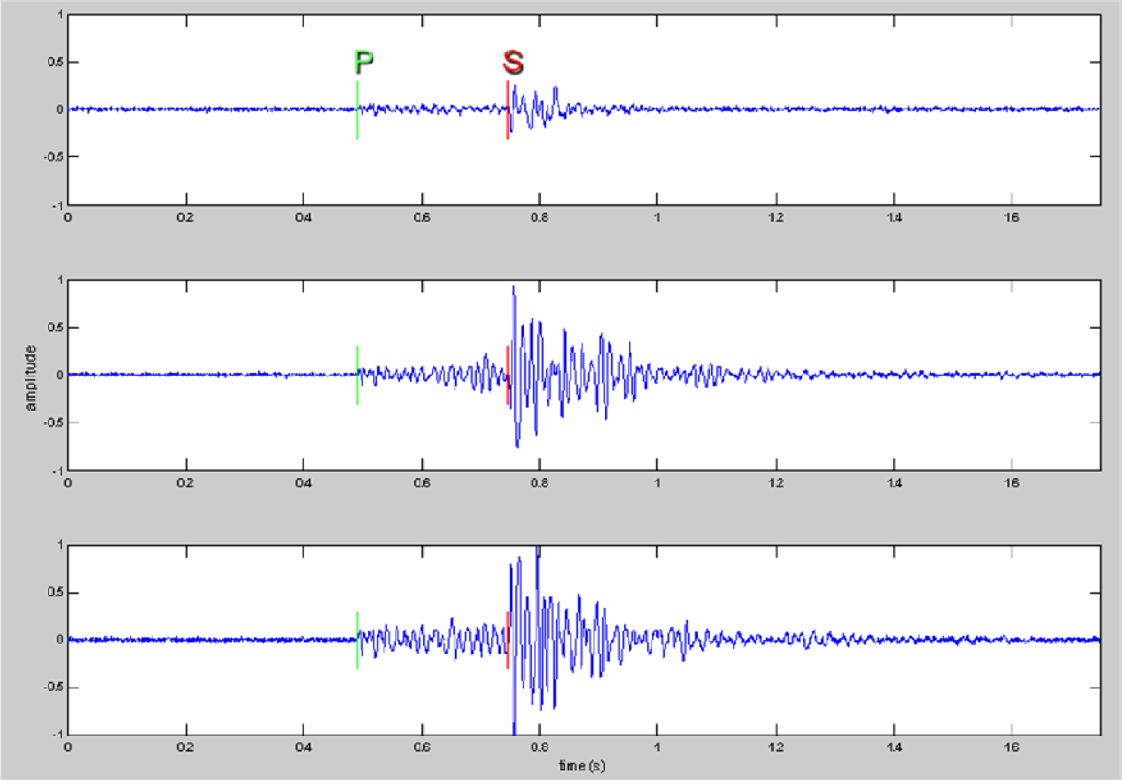

Figure 3. Three components of seismic waveform from an induced event detected by the borehole network, along with the P and S-phase picks.

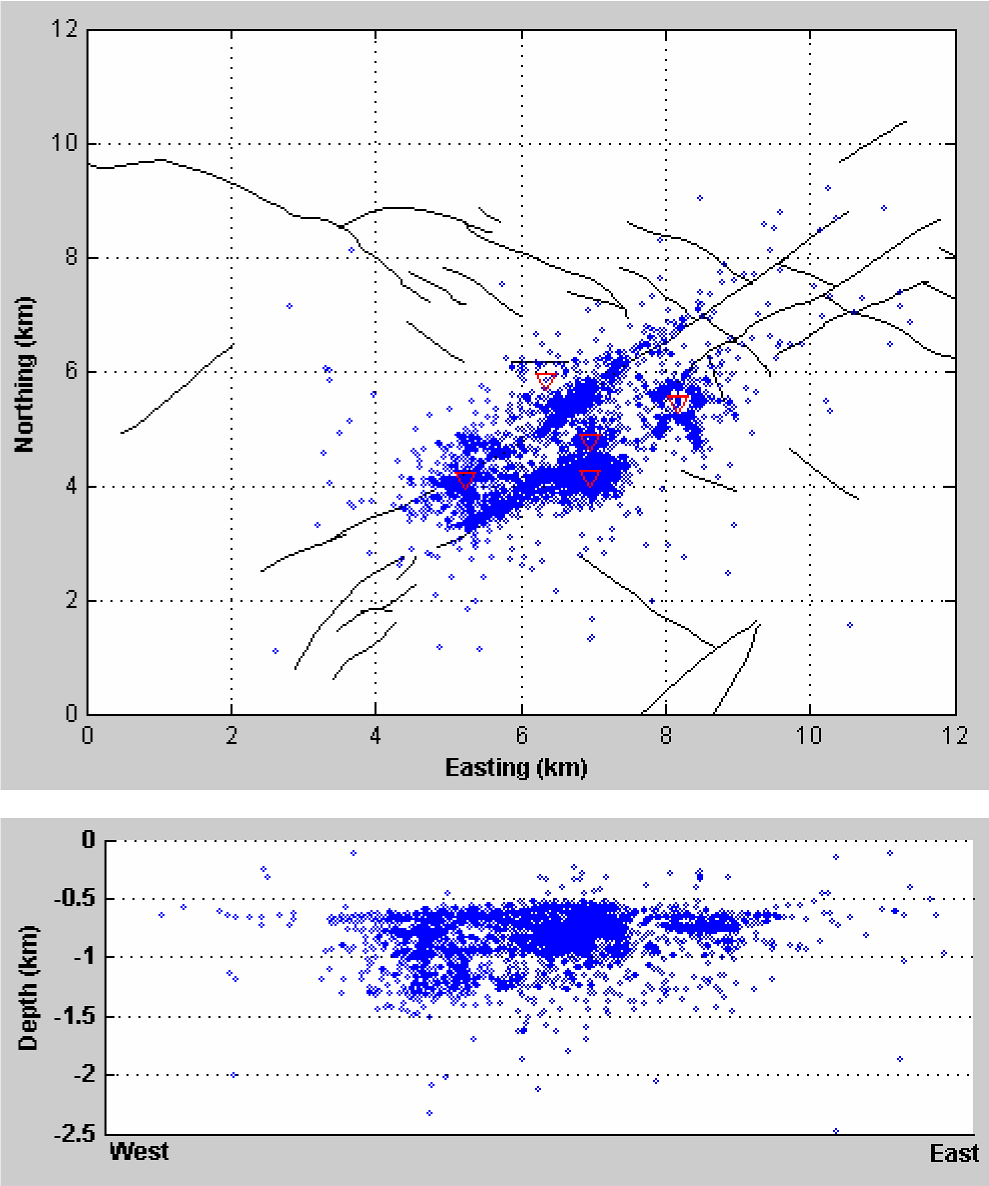

Figure 4. Location of induced seismic events occurring every other day during the period Oct 2002 – Aug 2003. Top: event epicenters (blue dots), with fault maps derived from surface seismic at Natih horizon (black lines) and surface coordinates of the monitoring wells (red triangles). Bottom: depth distribution of the events along a vertical plane (East-West section). The length of the West to East axis shown on this plot is 9 km (corresponding to a profile line extending from 2 to 11 km along the Easting axis of the top plot).

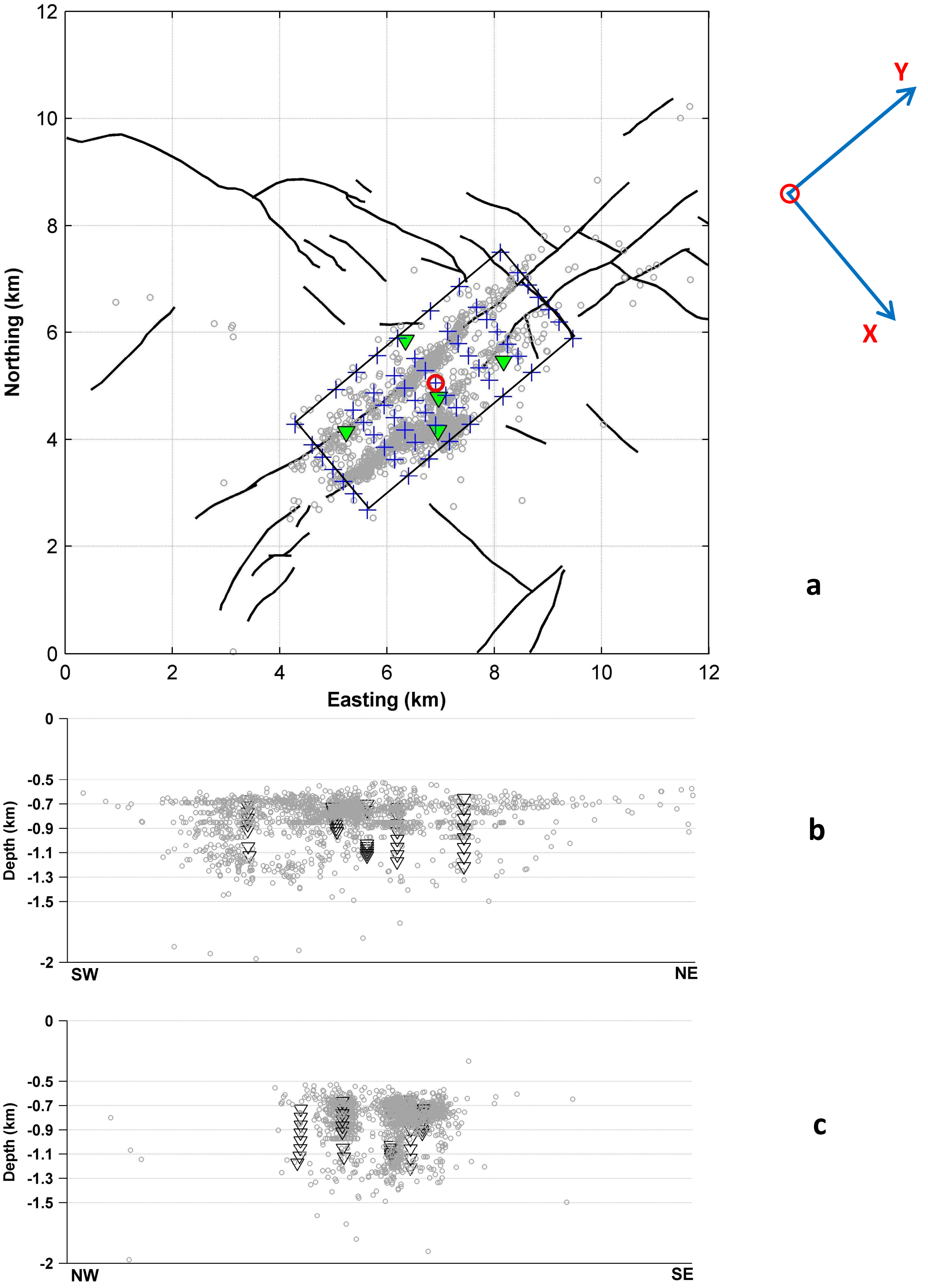

Figure 5. (a) Setup for double-difference tomography using borehole network data in map view: events (grey dots), stations (triangles), inversion grids (blue "+" symbols), the center of the rotated coordinate system (red circle), and fault traces (black lines). Also shown is a schematic diagram of the rotated coordinated system on the right. (b) Depths of events (grey dots) shown along strike (NE-SW) and normal to the major strike (NW-SE) direction.

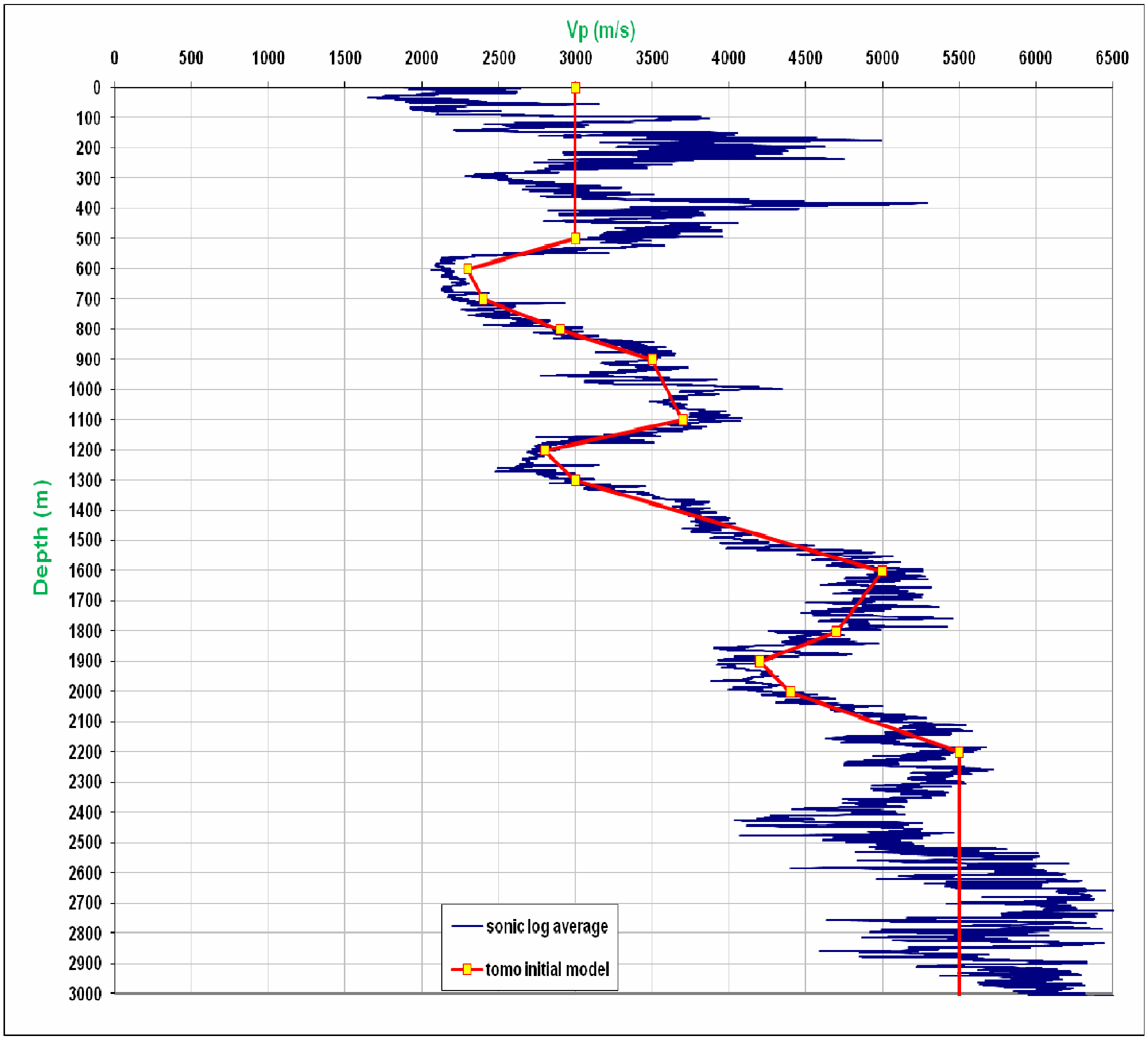

Figure 6. Initial P-wave velocity model for depth nodes shown by yellow squares. For travel time calculation, the velocity between two nodes is linearly interpolated – as shown by the red curves. Blue curve shows an average Vp derived from five Sonic logs, which serves as a guideline for selecting the depth nodes for inversion and the corresponding starting velocities.

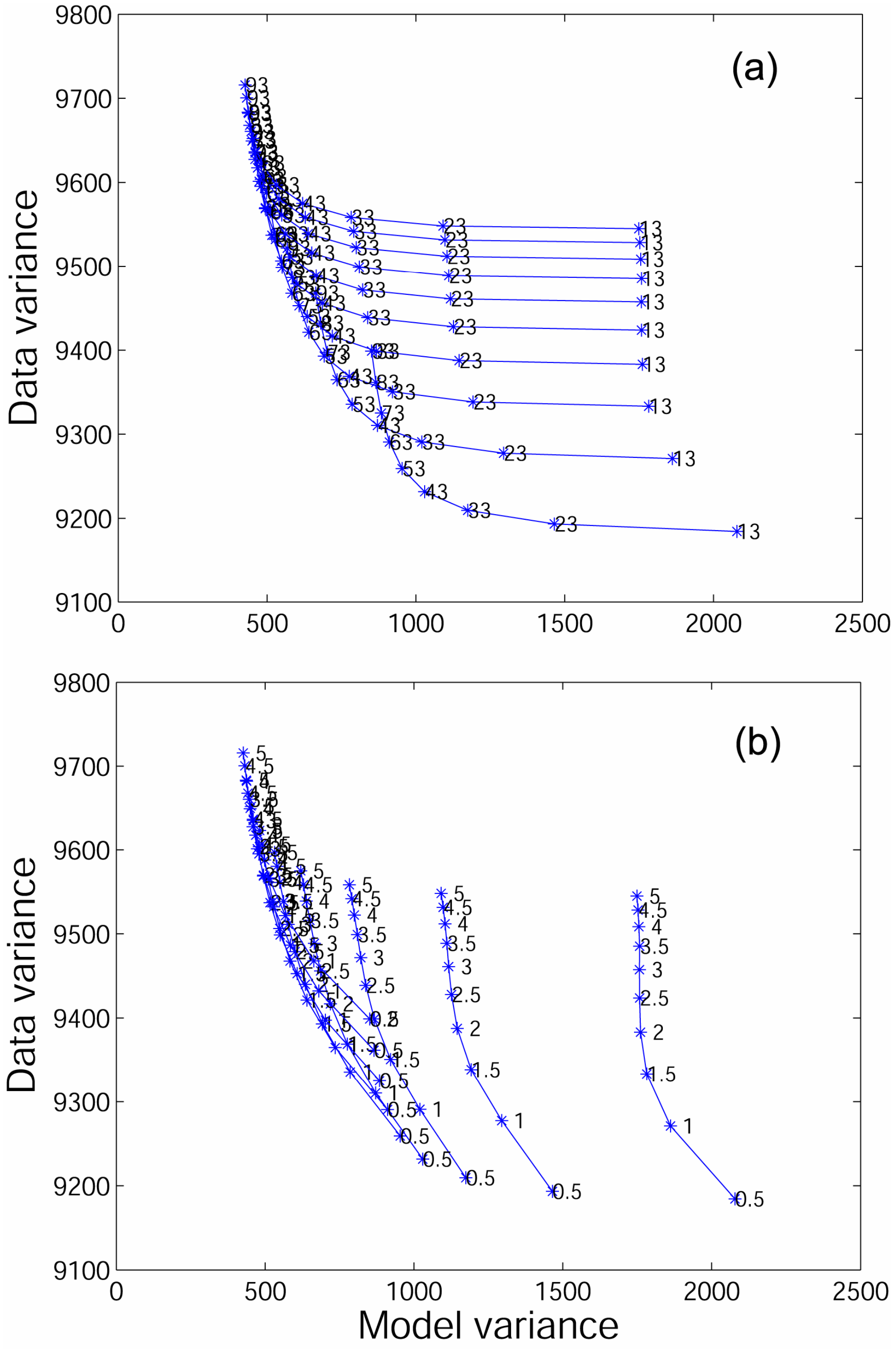

Figure 7. Trade-off analysis of data variance and model variance for a series of damping values from 13 to 93 and smooth weighting values of 0.5 to 5. (a) Trade-off curves for different smooth weighting values. (b) Trade-off curves for different damping values. The selected smooth weighting and damping values are 1.5 and 35.

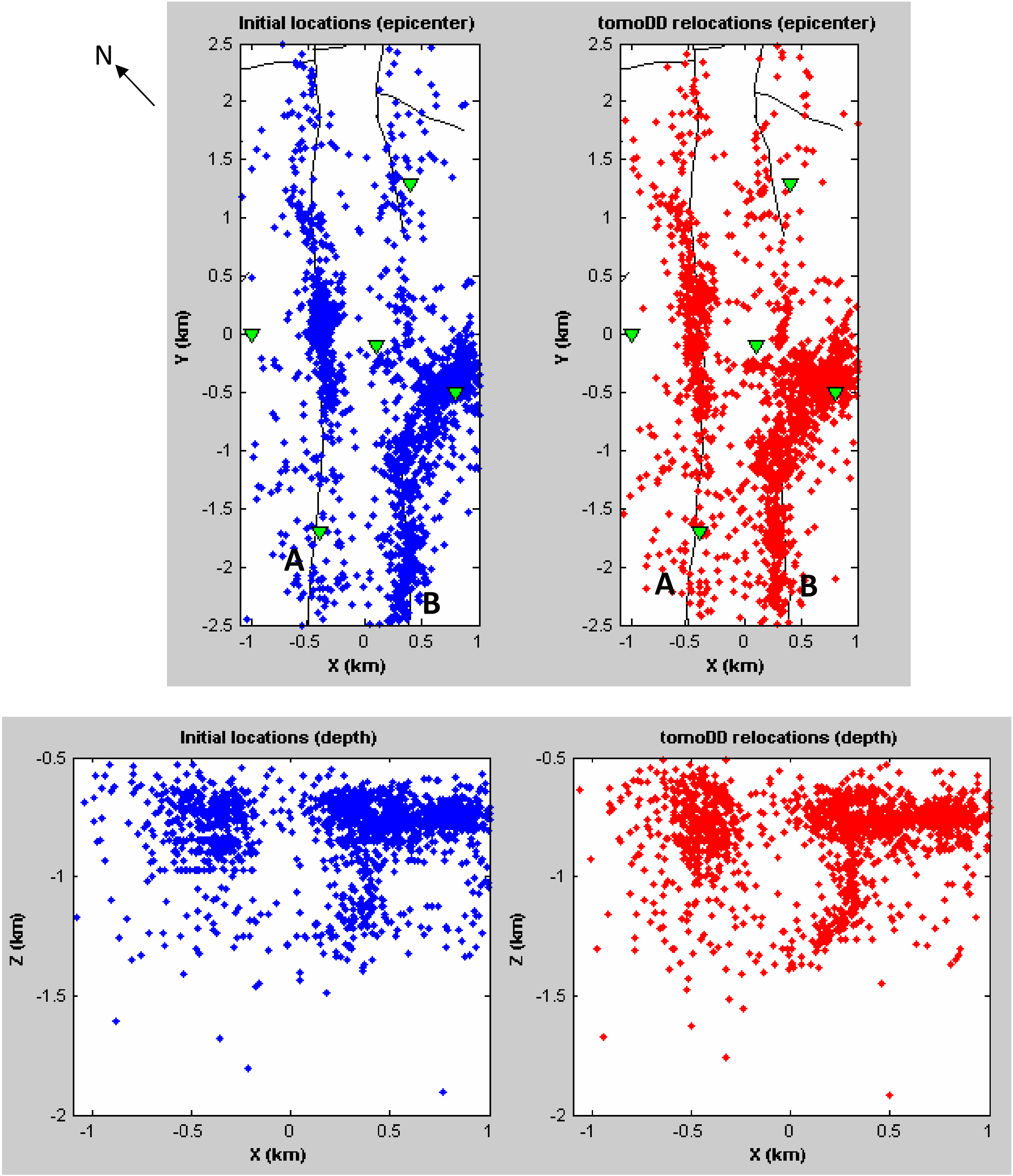

Figure 8. Comparison of initial (blue dots) and double-difference tomography relocations (red dots) of induced events used for reservoir imaging. Event locations are plotted for the rotated coordinate system (as shown by Figure 5). On the epicenter map, black lines and green triangles show existing faults and locations of monitoring wells (boreholes), respectively.

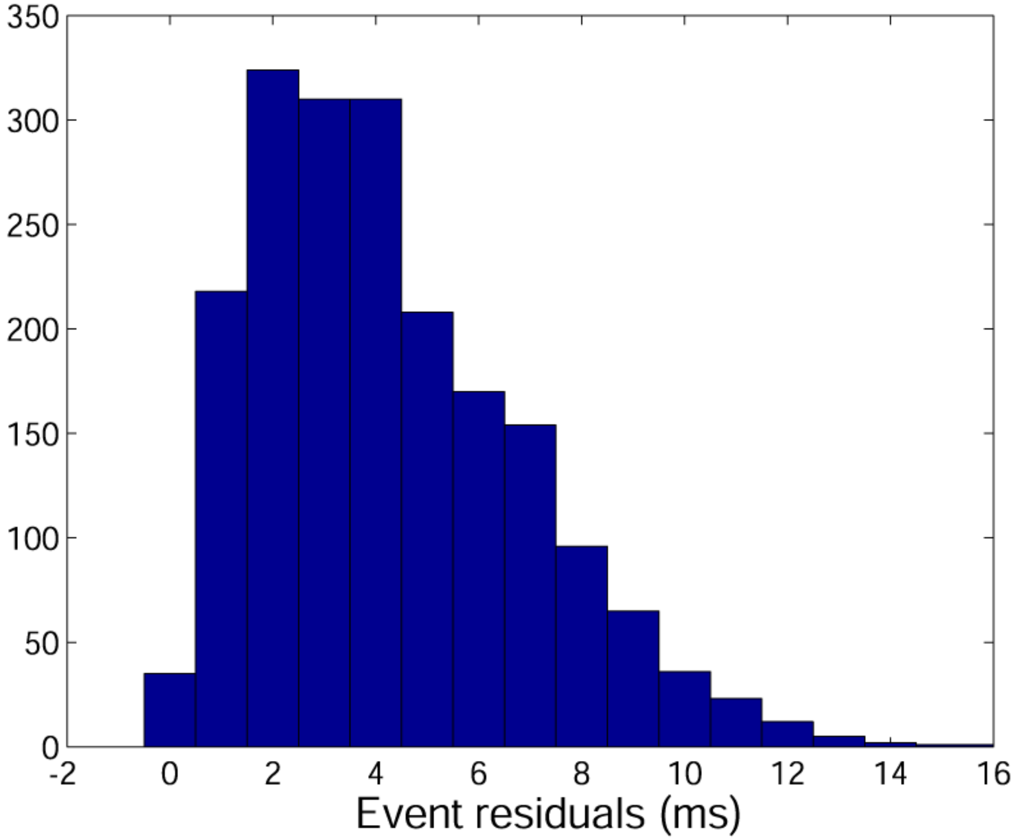

Figure 9. Histogram of RMS travel time residuals for events based on final velocity models and event locations from double-difference tomography.

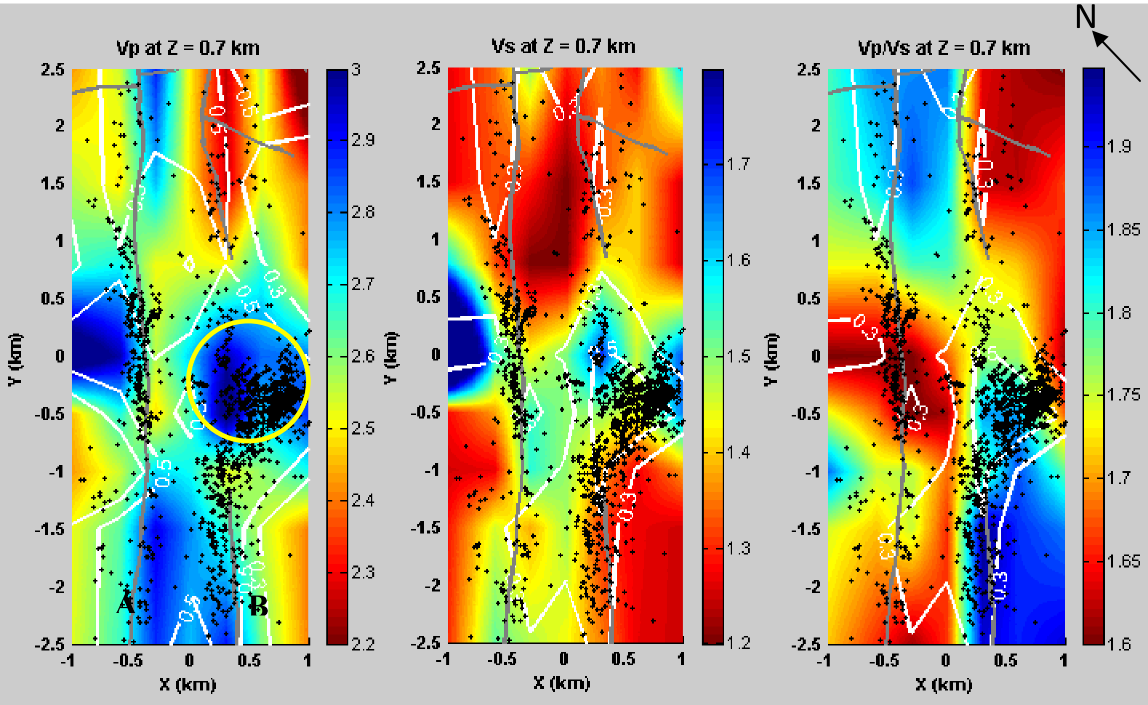
Vp at Z = 0.7 km
Vs at Z = 0.7 km
Vp/Vs at Z = 0.7 km
N
Y (km)
X (km)
A
B
2.5
2
1.5
1
0.5
0
-0.5
-1
-1.5
-2
-2.5
-1
-0.5
0
0.5
1
3
2.9
2.8
2.7
2.6
2.5
2.4
2.3
2.2
1.7
1.6
1.5
1.4
1.3
1.2
1.9
1.85
1.8
1.75
1.7
1.65
1.6
0.5
0.3

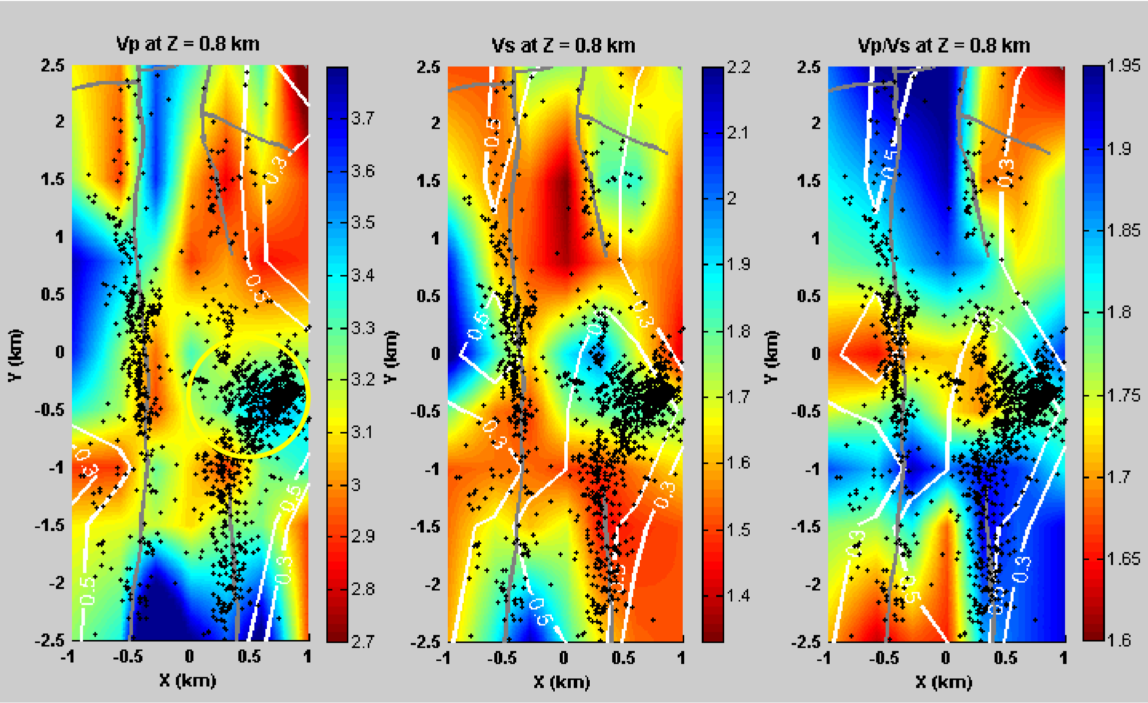
Vp at Z = 0.8 km
Vs at Z = 0.8 km
Vp/Vs at Z = 0.8 km
Y (km)
X (km)
2.5
2
1.5
1
0.5
0
-0.5
-1
-1.5
-2
-2.5
-1
-0.5
0
0.5
1
3.7
3.6
3.5
3.4
3.3
3.2
3.1
3
2.9
2.8
2.7
2.2
2.1
2
1.9
1.8
1.7
1.6
1.5
1.4
1.95
1.9
1.85
1.8
1.75
1.7
1.65
1.6
0.5
0.3

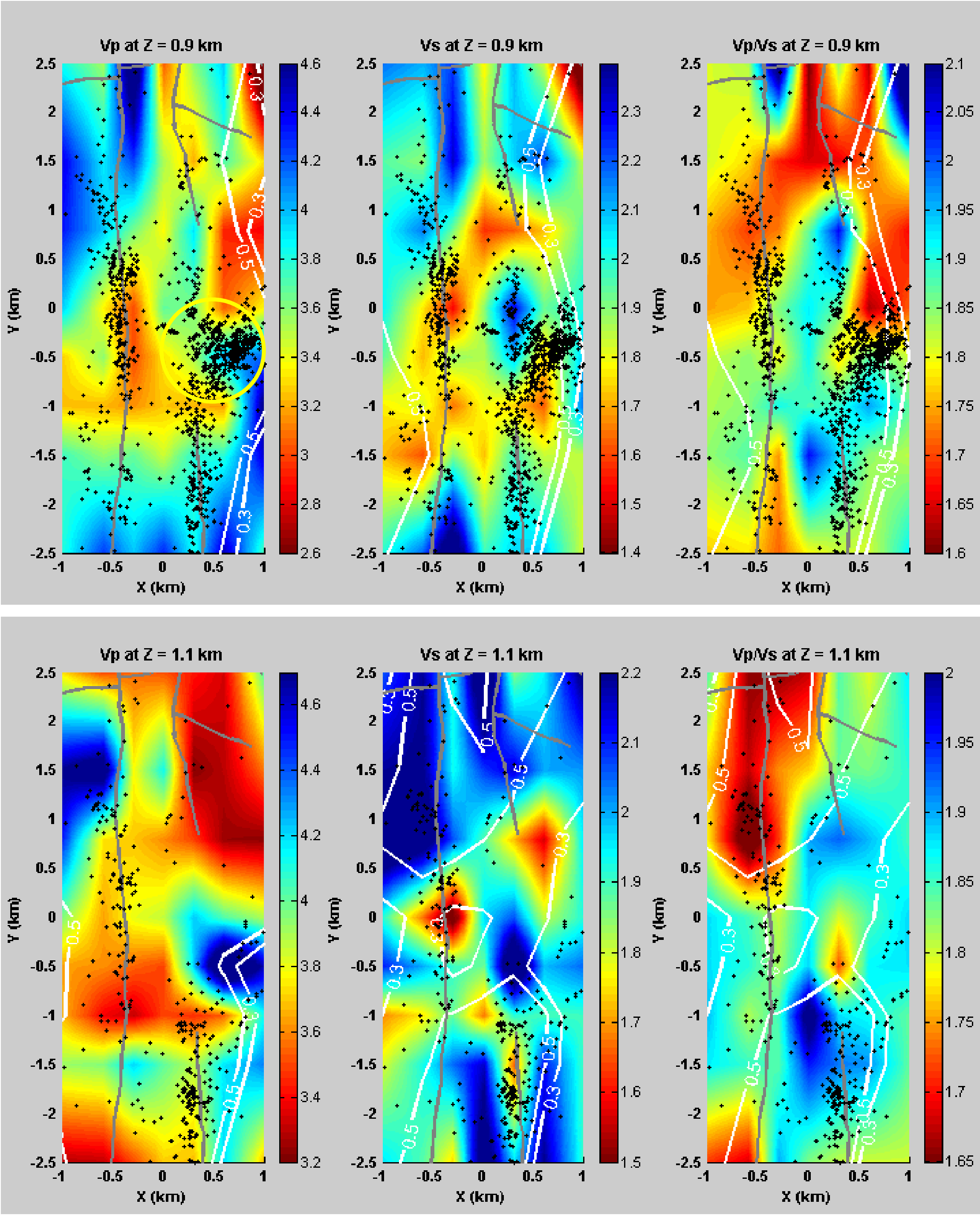

Figure 10. Horizontal slices of the three-dimensional Vp, Vs, and Vp/Vs models (column-wise, from left to right) at different depths. Included in the plots are preexisting fault maps derived at Natih horizon from surface seismic (grey lines), induced seismicity locations for ± 100 m depth of each section plot (black dots), and the resolution contours obtained from the resolution matrix (white). As per the resolution matrix test, only the regions that have resolution values > 0.3 are considered for interpretation.

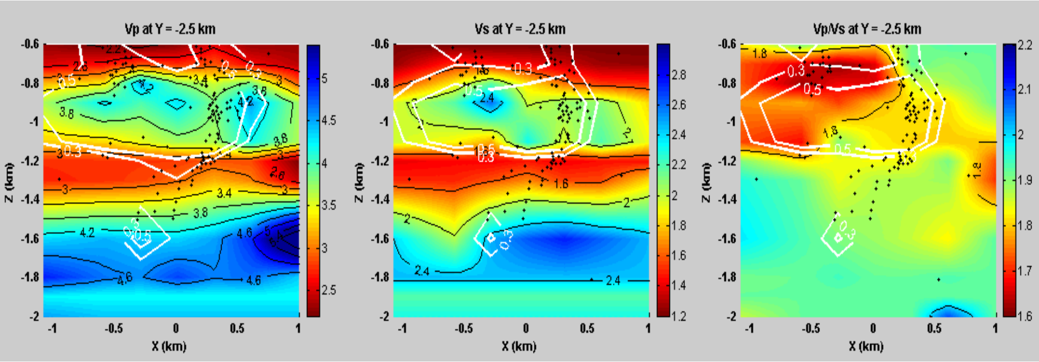
Vp at Y = -2.5 km
Vs at Y = -2.5 km
Vp/Vs at Y = -2.5 km
Z (km)
X (km)

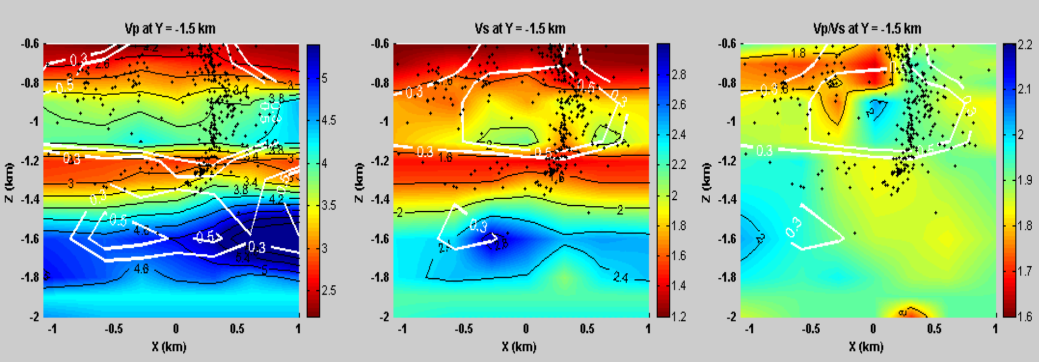
Vp at Y = -1.5 km
Vs at Y = -1.5 km
Vp/Vs at Y = -1.5 km
Z (km)
X (km)

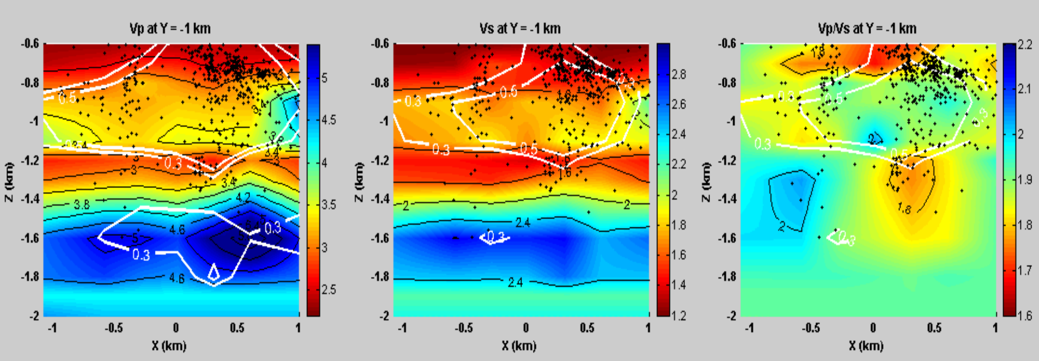
Vp at Y = -1 km
Vs at Y = -1 km
Vp/Vs at Y = -1 km
Z (km)
X (km)

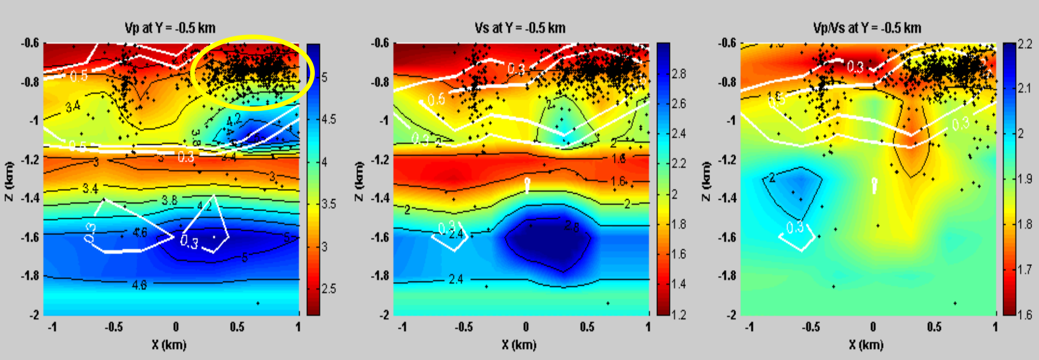
Vp at Y = -0.5 km
Vs at Y = -0.5 km
Vp/Vs at Y = -0.5 km
Z (km)
X (km)

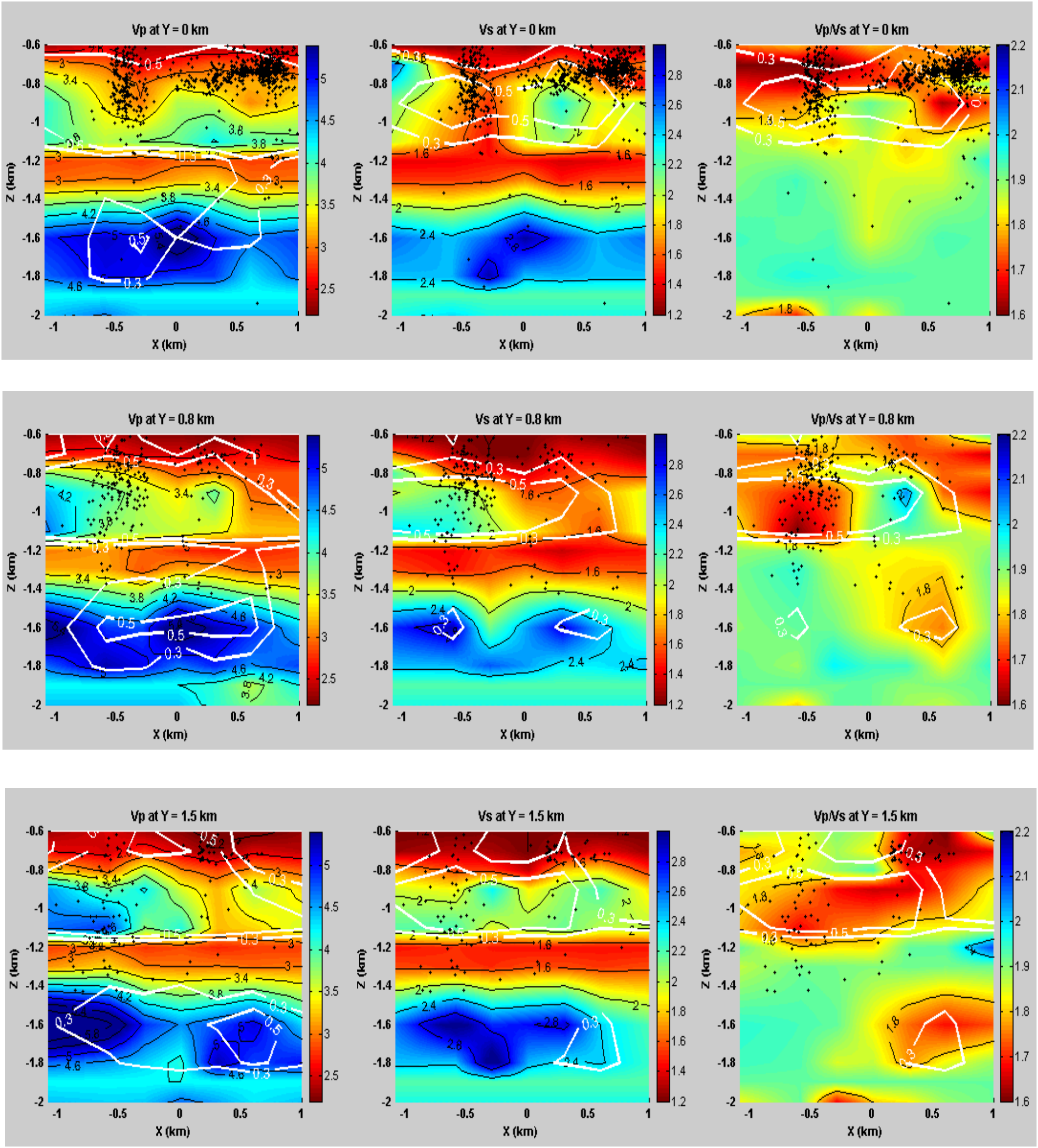

Figure 11. Across-fault cross sections of Vp, Vs, and Vp/Vs (column-wise, from left to right) at different Y locations. Also shown on the plots in black are the contour lines and labels of the variables. Induced seismicity locations (black dots) within ± 500 m of each section are superimposed on the velocity images. Also, the resolution contours obtained from the resolution matrix are superimposed in white. On each of these images, regions where the resolution values are greater than 0.3 can be used for interpretation.

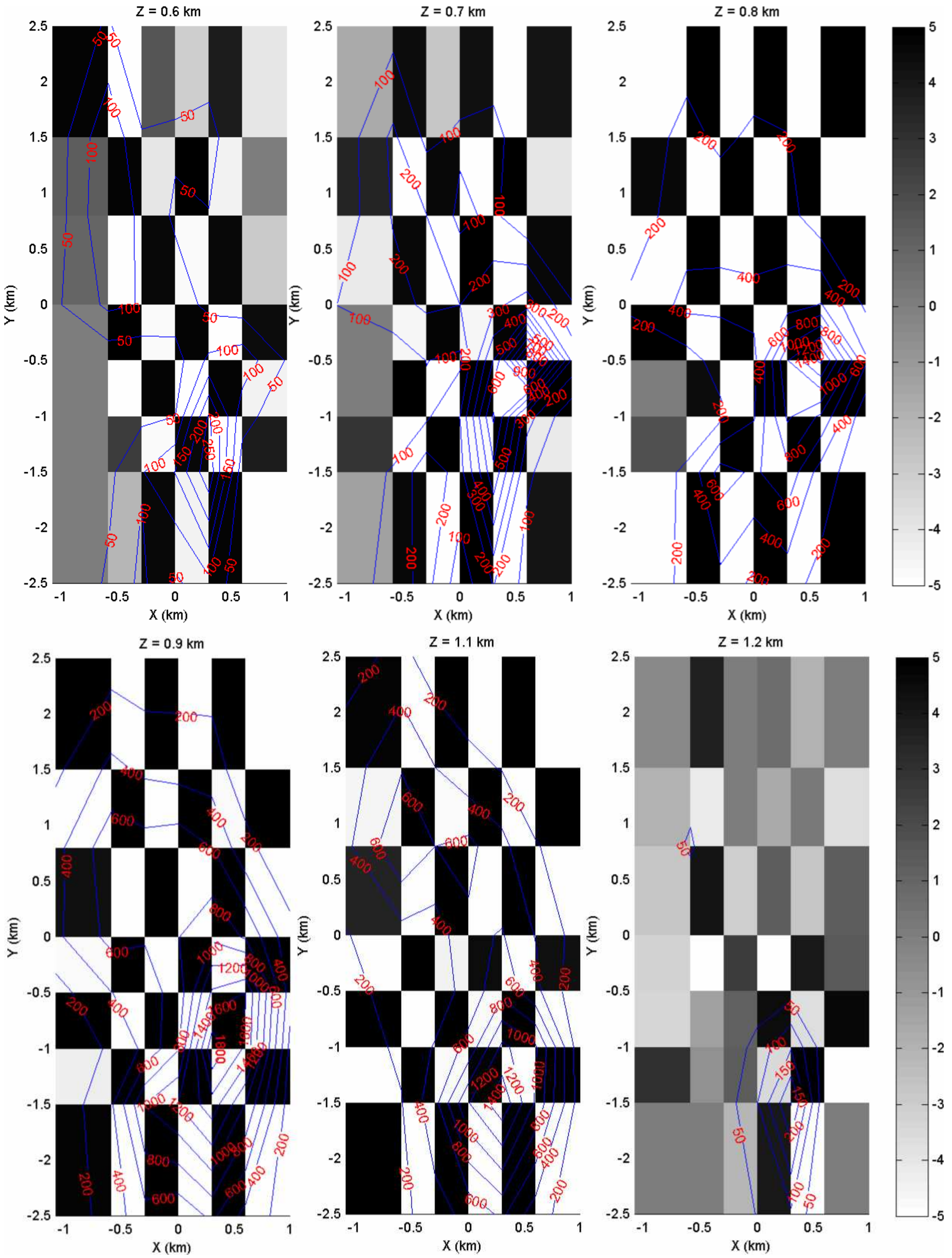

Figure A1. Inverted checkerboard patterns at different depths. DWS contours from inversion are plotted in blue and labeled in red.

Resolution contours for Vp at Z = 0.5 km

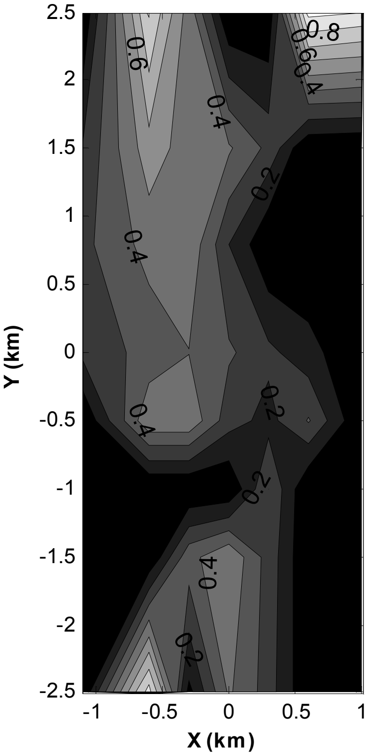

Resolution contours for Vs at Z = 0.5 km

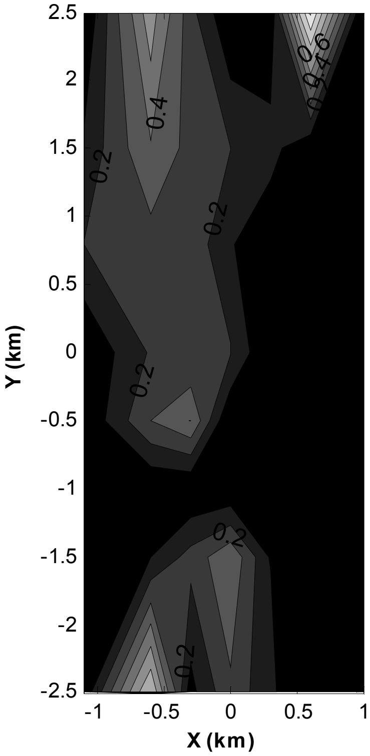

Resolution contours for Vp at Z = 0.6 km

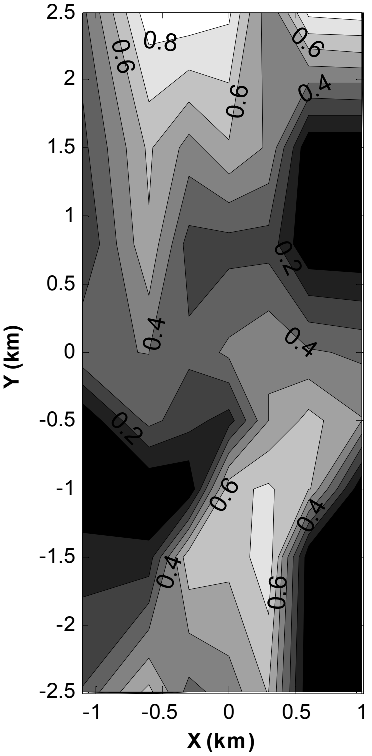

Resolution contours for Vs at Z = 0.6 km

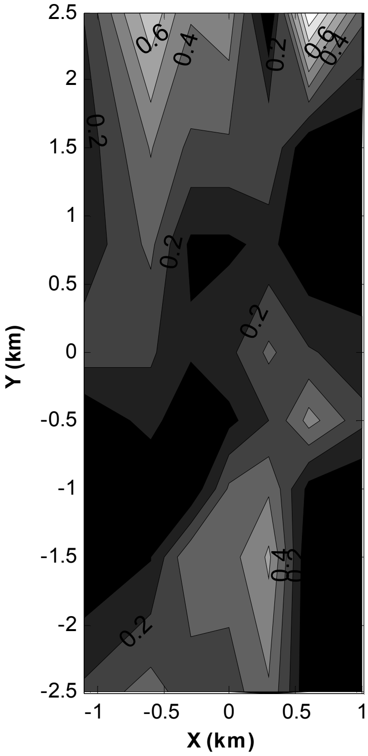

Resolution contours for Vp at Z = 0.7 km

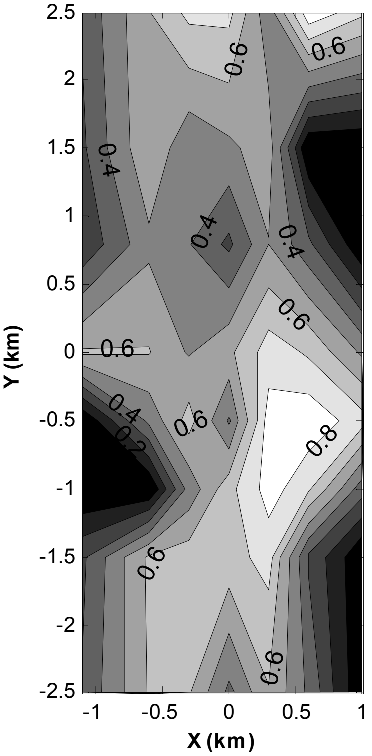

Resolution contours for Vs at Z = 0.7 km

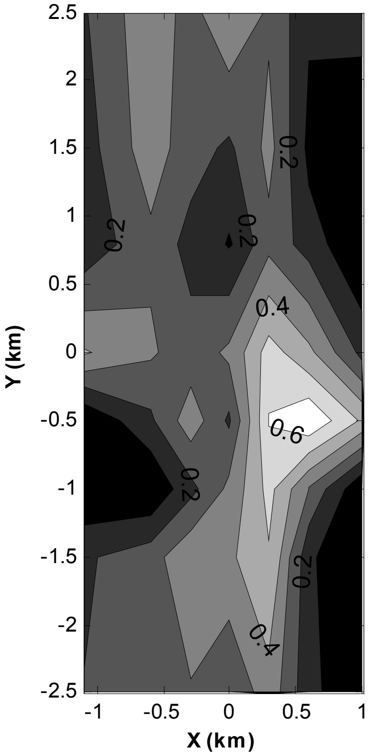

Resolution contours for Vp at Z = 0.8 km

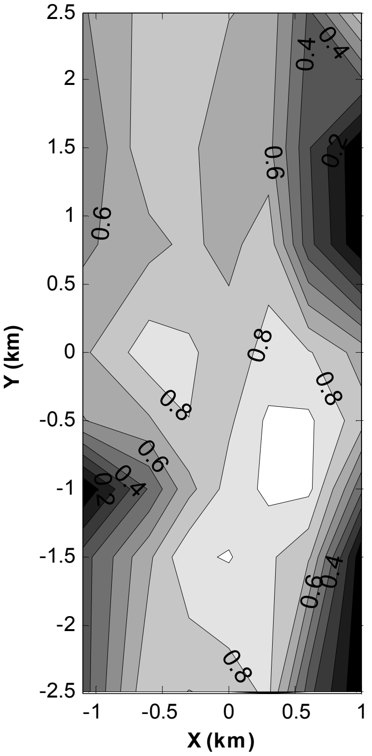

Resolution contours for Vs at Z = 0.8 km

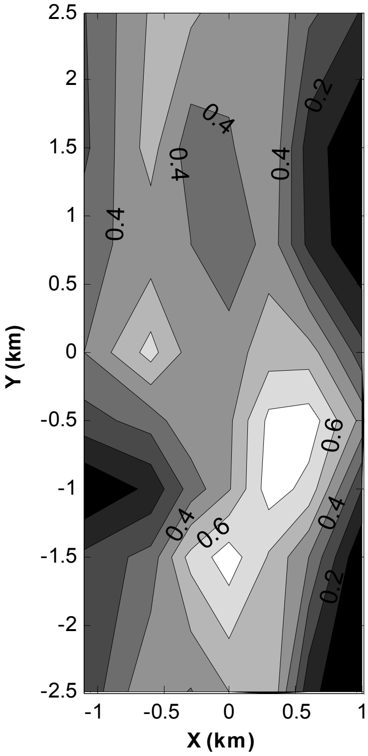

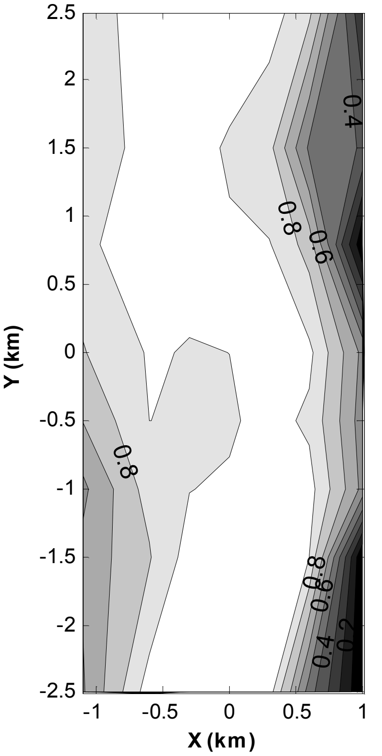

Resolution contours for Vp at Z = 0.9 km

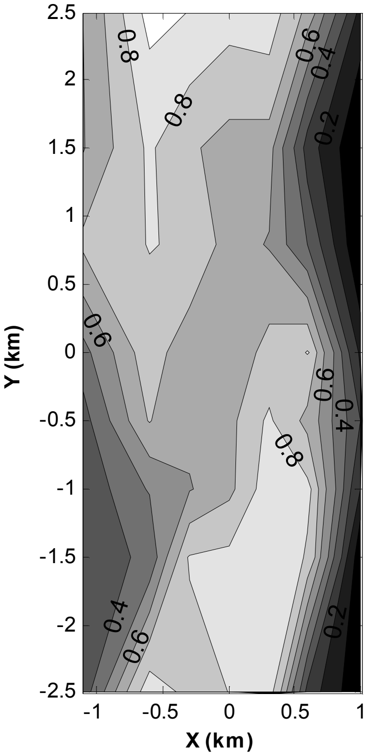

Resolution contours for Vs at Z = 0.9 km

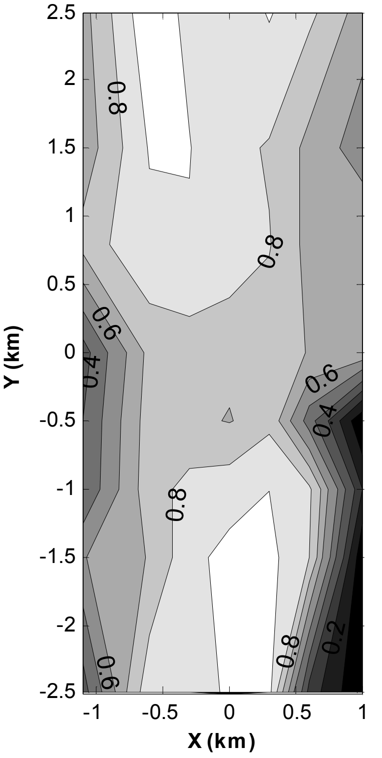

Resolution contours for Vp at Z = 1.1 km

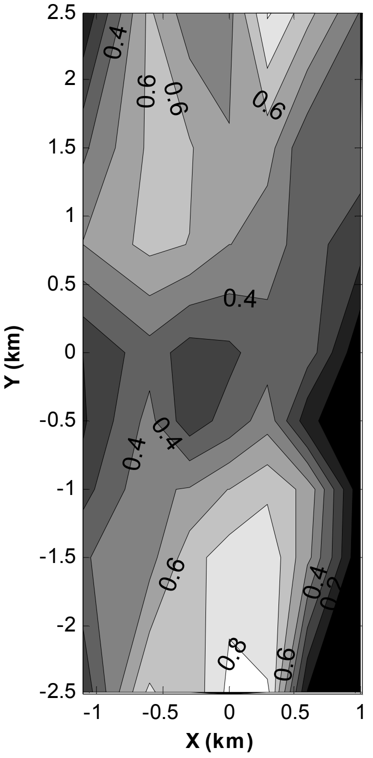

Resolution contours for Vs at Z = 1.1 km

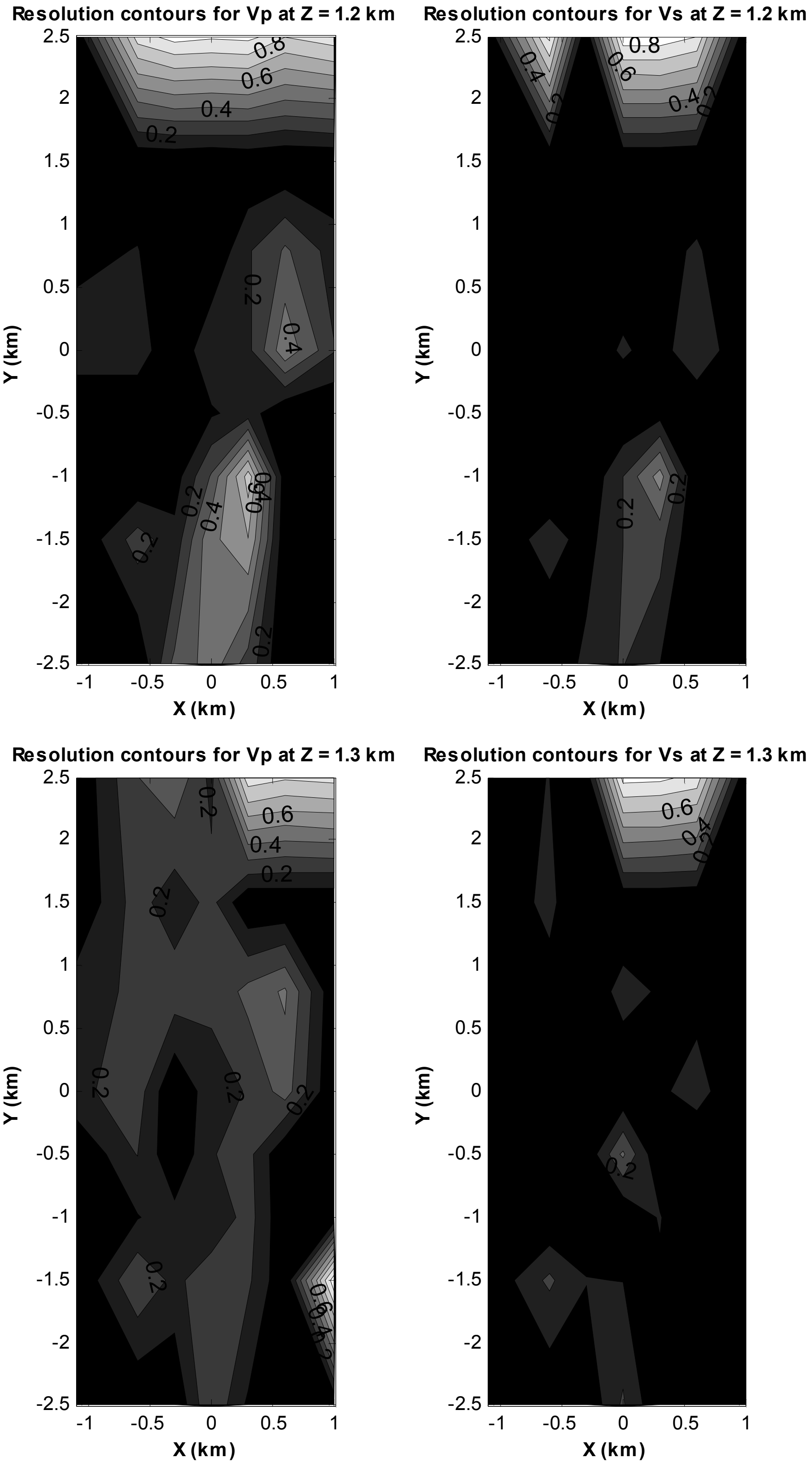

Figure A2. Resolution contours for Vp and Vs models at different depths.

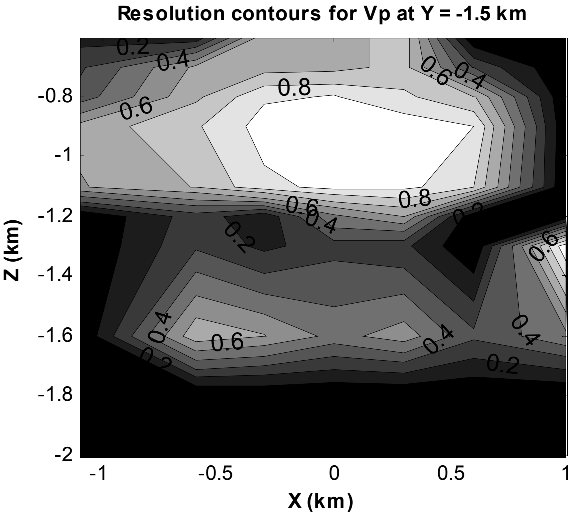

Resolution contours for Vp at Y = -1.5 km

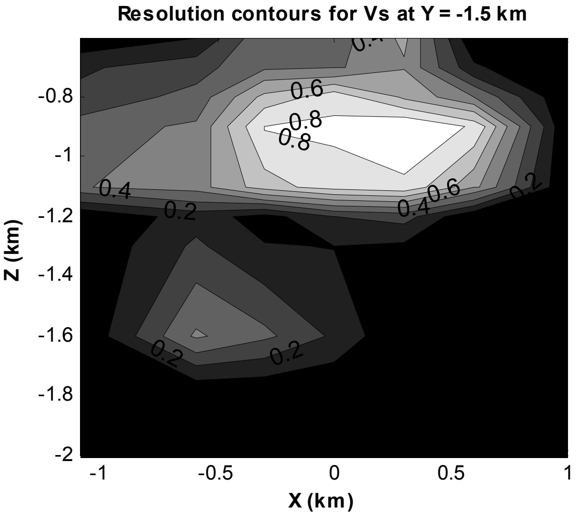

Resolution contours for Vs at Y = -1.5 km

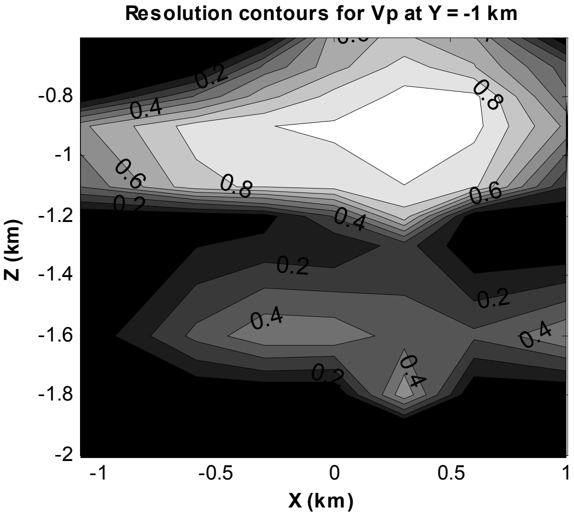

Resolution contours for Vp at Y = -1 km

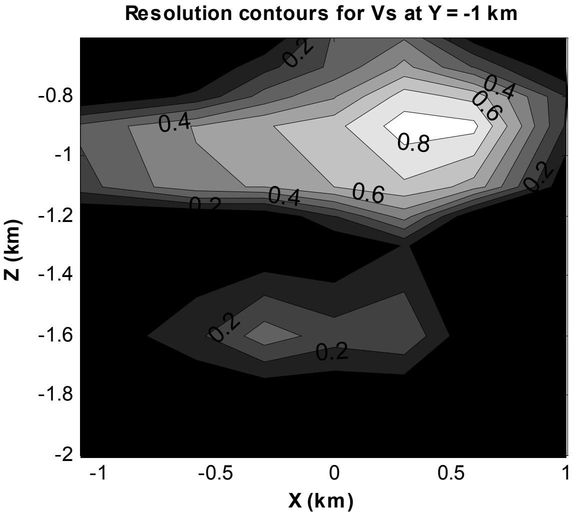

Resolution contours for Vs at Y = -1 km

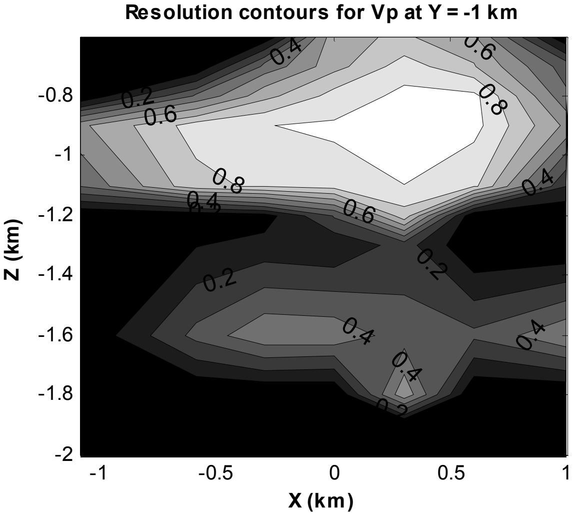

Resolution contours for Vp at Y = -1 km

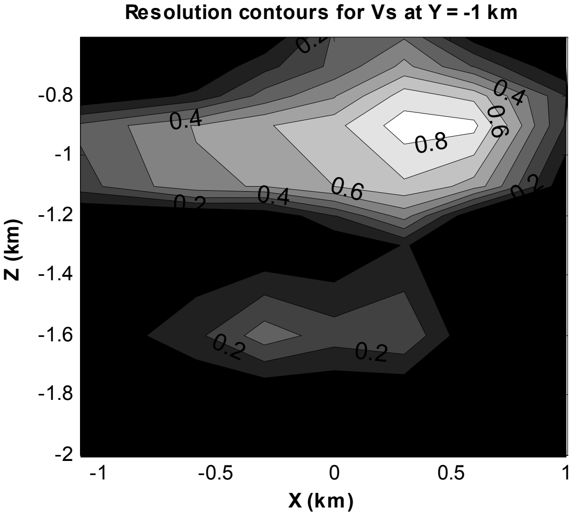

Resolution contours for Vs at Y = -1 km

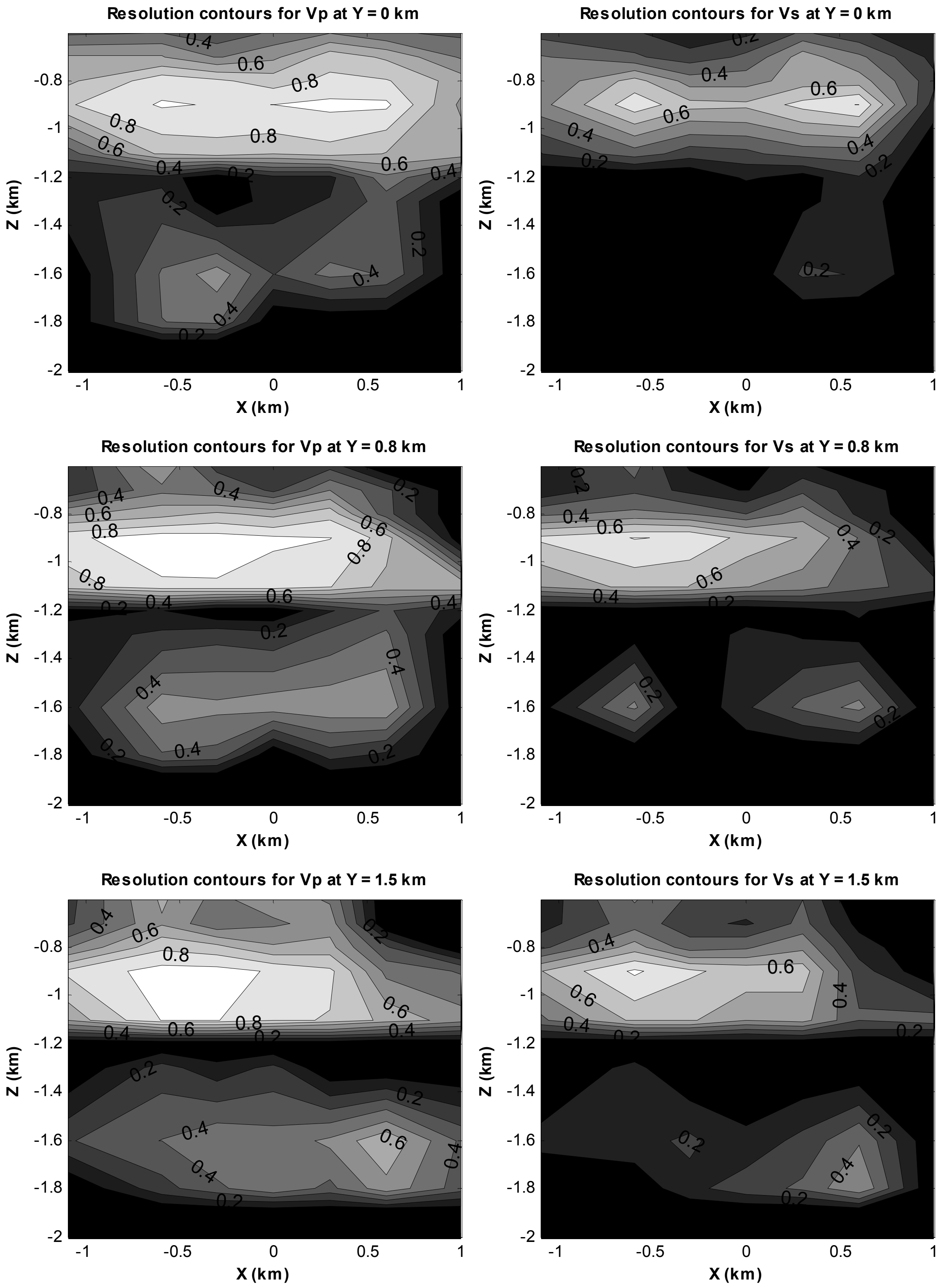
Resolution contours for Vp at Y = 0 km

Resolution contours for Vs at Y = 0 km

Resolution contours for Vp at Y = 0.8 km

Resolution contours for Vs at Y = 0.8 km

Resolution contours for Vp at Y = 1.5 km

Resolution contours for Vs at Y = 1.5 km

Figure A3. Diagonal resolution contours for the across-fault cross sections at Y=-1.5, -1, -0.5, 0, 0.8, and 1.5 km. The model is likely to be resolved in places where the contour is greater than 0.3.

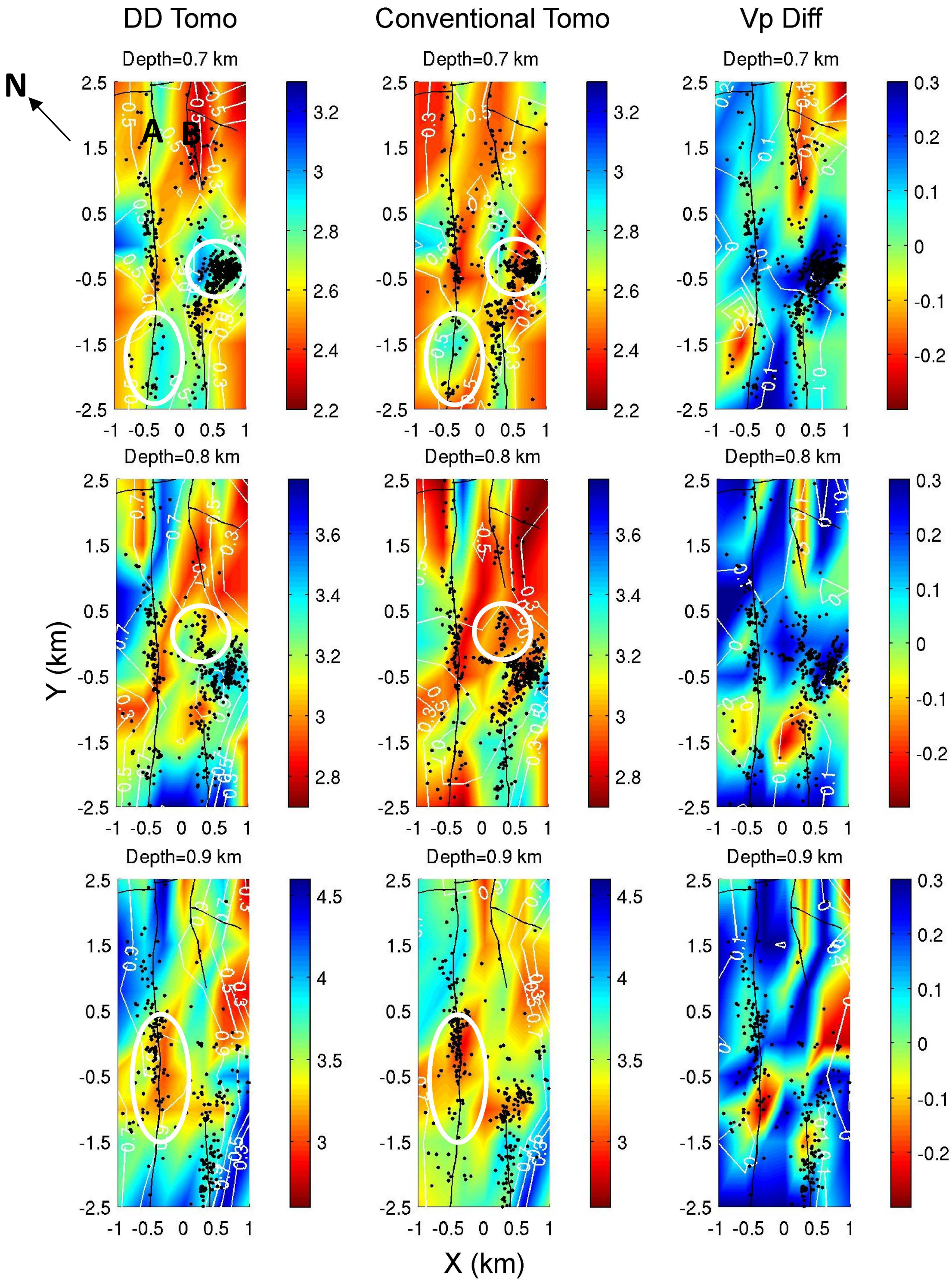

Figure A4. Comparison of Vp models at depths 0.7, 0.8 and 0.9 km from DD tomography and conventional tomography. (Left) DD tomography Vp models and event locations with diagonal resolution matrix values plotted in white contours; (Middle) Conventional tomography Vp models and event locations with diagonal resolution matrix values plotted in white contours; (Right) Vp differences with event locations from DD tomography. White contours indicate the resolution differences.